

Combined Experimental and Computational Approach toward the Structural Design of Borosilicate-Based Bioactive Glasses

Nicholas Stone-Weiss, Henrik Bradtmüller, Mariagrazia Fortino, Marco Bertani, Randall E. Youngman, Alfonso Pedone, Hellmut Eckert,* and Ashutosh Goel*



Cite This: <https://dx.doi.org/10.1021/acs.jpcc.0c04470>



Read Online

ACCESS |



Metrics & More

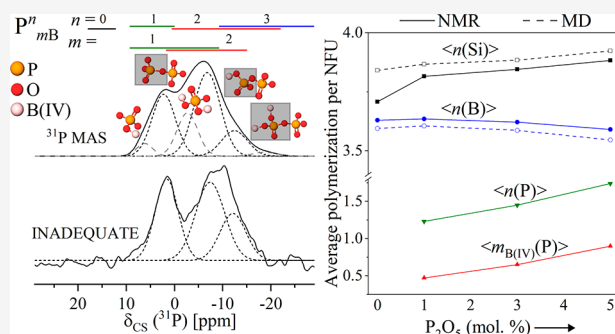


Article Recommendations



Supporting Information

ABSTRACT: Transitioning beyond a *trial-and-error* based approach for the compositional design of next-generation borosilicate-based bioactive glasses requires a fundamental understanding of the underlying compositional and structural drivers controlling their degradation and ion release *in vitro* and *in vivo*. Accordingly, the present work combines magic-angle spinning (MAS) NMR techniques, MD simulations, and DFT calculations based on GIPAW and PAW algorithms, to build a comprehensive model describing the short-to-medium-range structure of potentially bioactive glasses in the $\text{Na}_2\text{O}-\text{P}_2\text{O}_5-\text{B}_2\text{O}_3-\text{SiO}_2$ system over a broad compositional space. P_2O_5 preferentially tends to attract network modifier species, thus resulting in a repolymerization of the silicate network and a restructuring of the borate component. $^{11}\text{B}\{^{31}\text{P}\}$ and $^{31}\text{P}\{^{11}\text{B}\}$ dipolar recoupling experiments suggest that the ability of glasses to incorporate P_2O_5 without phase separation is related to the formation of P–O–B(IV) linkages integrated into the borosilicate glass network. An analogous approach is used for elucidating the local environments of the Na^+ network modifiers. This work, along with future studies aimed at elucidating *composition–structure–solubility/bioactivity* relationships, will lay the foundation for the development of quantitative structure–property relationship (QSPR) models, thus representing a leap forward in the design of functional borosilicate bioactive glasses with controlled ionic release behavior.



1. INTRODUCTION

The concept of designing third-generation biomaterials is based on the principle of activating a synchronized sequence of genes at the cellular level by the ionic dissolution products released from the biomaterial during its controlled degradation *in vitro* or *in vivo*. While second-generation biomaterials are designed to be either resorbable or bioactive, these two properties are combined in the third-generation materials, which will, upon implantation, help the body heal itself.¹

While the 45S5 Bioglass composition (24.3Na₂O–26.9CaO–2.6P₂O₅–46.1SiO₂, mol %), was initially developed as a second-generation biomaterial, the ability of its ionic dissolution products to stimulate genetic responses in the processes relevant to osteoblast metabolism and bone homeostasis has paved the way for its application as third-generation biomaterial.^{2–4} However, owing to its high tendency toward devitrification (resulting in poor sintering ability—a prerequisite to fabricate 3D porous scaffolds)^{5–8} and slow/poor resorbability, due to the formation of a Si–OH-based passivating gel layer on its surface when in contact with body fluids,⁹ its application as a third-generation biomaterial has been confined to its use as fine powders/particulates present in toothpaste and dental putty.¹⁰ Therefore, in order to suppress its tendency toward devitrification, and improve its resorbability, B₂O₃ was introduced into

the silicate network of 45S5 Bioglass, thus resulting in the emergence and development of borosilicate-based bioactive glasses.^{11–15}

The past 15+ years have experienced a tremendous upsurge in the research interest of boron-containing bioactive glasses as potential candidates for the design and development of novel third-generation biomaterials.^{16–18} Borosilicate glasses, in particular, provide certain advantages over standard silicate-based compositions, including (i) a broader glass-forming range, (ii) tunable degradation rates,¹⁶ and (iii) ease of processing into porous three-dimensional scaffolds for application in tissue engineering.^{17,19} Recent studies have further shown their ability to promote angiogenesis and osteogenesis *in vivo*.^{11,16} These features make borosilicate-based bioactive glasses an attractive candidate for application in the treatment of a broad range of skeletal and nonskeletal biomedical problems. However, a major problem that impedes the design of novel borosilicate-based

Received: May 18, 2020

Revised: July 16, 2020

Published: July 16, 2020

bioactive glasses is our poor understanding of the underlying compositional and structural drivers controlling borosilicate dissolution kinetics when in contact with body fluids. This knowledge gap stems from the fact that the vast majority of research in the field of bioactive glasses have focused on silicate glasses, either based on—or inspired by—45S5 Bioglass.^{20–25} Furthermore, as explained in the next section, the principles of silicate glass dissolution/degradation (e.g., *composition–structure–bioactivity* correlations) generally do not apply to borate or borosilicate glasses. As a consequence, the design of borate and borosilicate glasses—especially those that exhibit the desired dissolution behavior—has followed Edisonian approaches involving time-consuming and iterative synthesis-testing cycles. Two notable examples are 13-93B1 and 13-93B3 glasses, derived from a well-known silicate-based bioactive glass (13-93). These compositions have been designed through a *trial-and-error* approach in the series $6.0\text{Na}_2\text{O}-7.9\text{K}_2\text{O}-7.7\text{MgO}-22.1\text{CaO}-1.7\text{P}_2\text{O}_5-x\text{B}_2\text{O}_3-(54.6-x)\text{SiO}_2$ (mol %), where $x = 0$ is 13-93 and $x = 18.2$ and 54.6 are 13-93B1 and 13-93B3 compositions, respectively. This partial or complete replacement of SiO_2 with B_2O_3 was performed with little rationale or revelation of the underlying *composition–structure–property* relationships.^{26,27} For a more efficient design of such functional materials, we will require a deeper, more fundamental understanding of the compositional and structural dependence of glass degradation behavior *in vitro* and *in vivo*.

2. WHY CAN WE NOT APPLY OUR UNDERSTANDING OF THE STRUCTURE OF SILICATE-BASED BIOACTIVE GLASSES TO DESIGN BOROSILICATE GLASSES WITH CONTROLLED ION-RELEASE?

The discovery of 45S5 Bioglass was a paradigm shift in the field of biomaterials which later became a benchmark for subsequent research in the field of bioactive glasses. Based on our understanding of the structure and bioactivity of 45S5 Bioglass, the highest bioactivity in silicate-based bioactive glasses arises from a structure dominated by metasilicate chains (Si^2 units), which are occasionally cross-linked through Si^3 units, and are terminated with Si^1 species.²⁸ Here, and throughout the text, T^n_{mX} (T , $\text{X} = \text{Si}, \text{B}, \text{P}$) refers to the network former unit (NFU) species, where n denotes the number of bridging oxygen (BO) atoms and $m \leq n$ specifies the number of linkages to other NFUs of type X . It should be noted here that when correlating the structural makeup of silicate glasses with their bioactivity, the latter was previously considered as the rate of formation of hydroxyapatite on the glass surface when in contact with body fluids.²¹ However, hydroxyapatite formation is no longer considered to be an initial marker of bioactivity and the ability to achieve a tunable degradation rate with controlled ion-release is instead a prerequisite for designing third-generation bioactive glasses suitable for tissue engineering.¹ Accordingly, silicate glasses with highly polymerized glass structures, for example, glasses consisting of high fractions of Si^3 or Si^4 units, may exhibit well-controlled ionic release properties while at the same time having lower bioactivity (i.e., glass 55S) or even becoming bioinactive (i.e., glass 65S).²¹ Furthermore, P_2O_5 , though not strictly necessary for bioactivity, plays a vital role in silicate glasses to enhance their bioactivity when present in small concentrations (for example, 2.5 mol % in 45S5 Bioglass). On a structural level, the enhanced bioactivity of P_2O_5 -containing silicate glasses has been attributed to the presence of loosely bound orthophosphate

units (P^0) in the glass structure whose relatively fast initial release from the glass into the solution enhances the bone-bonding ability of the glass.^{21,29,30}

When compared with the structure of silicate-based bioactive glasses, the structure of borosilicate-based glasses is much more complex.^{31,32} Similar to silicate-based glass chemistries, the dissolution behavior of borosilicate-based bioactive glasses is controlled by the short-to-medium-range order in the glass structure. As B_2O_3 enters the silica glass network, in addition to the introduction of new short-range order species (i.e., three- and four-coordinate boron species), the intermediate-range associations between NFUs in borosilicate glasses (e.g., $\text{Si}^4\text{O}-\text{B}^4$, $\text{Si}^4\text{O}-\text{B}^3$, $\text{B}^3\text{O}-\text{B}^4$, etc. linkages) further complicate the glass structure.^{33–36} These associations are expected to have a significant impact on the dissolution kinetics and bioactivity of these glasses. For instance, common boron NFU linkages in borosilicate glasses have lower enthalpies of hydrolysis, i.e., $\text{Si}^4\text{O}-\text{B}^3$ (-3.03 kJ/mol) and $\text{B}^3\text{O}-\text{B}^3$ (-16.98 kJ/mol), as compared to pure silica linkages ($\text{Si}^4\text{O}-\text{Si}^4$ linkages: 16.61 kJ/mol),³⁷ resulting in the greater degradation rates typically observed upon B_2O_3 substitution into silicate-based bioactive glasses.¹⁷ The addition of P_2O_5 further adds to the compositional and structural complexity of this glass system by forming $\text{B}-\text{O}-\text{P}$ linkages.^{38,39} The previously reported impacts of P_2O_5 additions to borosilicate glasses include an increased degree of polymerization of the silica and phosphate species and $\text{P}-\text{O}-\text{B}$ intermixing in the network.^{39–41} P_2O_5 is generally known as a cation scavenger in mixed network former glasses, attracting large amounts of modifier via multiple charged orthophosphate and diphosphate anions.^{38–40} However, the impact of these structural units and linkages on the dissolution kinetics of glasses is still largely unknown. Thus, it is difficult, if not impossible, to design next-generation borosilicate-based bioactive glasses using an approach based on the structure of silicate glasses.

In the context of the above-discussed rationale, the present contribution aims to combine the strengths of both experimental and computational materials science to uncover the short-to-medium-range structure of potentially bioactive glasses in the system $\text{Na}_2\text{O}-\text{P}_2\text{O}_5-\text{B}_2\text{O}_3-\text{SiO}_2$ system over a broad compositional space with distinct structural features. Although we understand that most bioactive glass compositions contain CaO as a major component, we have selected a calcium-free glass system for the following reasons:

- Competition between Na^+ and Ca^{2+} (i.e., in a $\text{Na}_2\text{O}-\text{CaO}-\text{P}_2\text{O}_5-\text{B}_2\text{O}_3-\text{SiO}_2$ system) nonframework cations for association with NFU units (B , P , Si) would add significant additional complexity while interpreting glass structural speciation.
- The structural role of Ca^{2+} in these glasses would be challenging to investigate in the absence of prior in-depth knowledge of the CaO -free system, given the extreme difficulty in measuring ^{43}Ca NMR spectra in glasses without an isotopic enrichment and/or an elevated Ca -presence in the sample.^{42–44} Additionally, the tendency of glasses containing both sodium and calcium to decrease the resolution of ^{29}Si and ^{31}P MAS NMR spectra further complicates their interpretation due to the creation of multiple chemical environments.²⁸
- The glass-forming ability of compositions containing both CaO and P_2O_5 is anticipated to be highly limited, due to the high cation field strength of Ca^{2+} and the high

Table 1. All Batched Compositions of Studied Glasses Compared to Selected Experimental Compositions (in Brackets), as Analyzed via ICP-OES (± 0.5 mol. %), with Density (ρ) and Molar Volume (V_M) Also Displayed

sample ID	batched				ρ (g/cm ³) ($\pm 0.3\%$)	V_M ($\pm 0.3\%$) (cm ³ /mol)
	Na ₂ O	P ₂ O ₅	B ₂ O ₃	SiO ₂		
PB0	25.0 [25.3]	—	30.0 [29.7]	45.0 [45.0]	2.519	25.18
PB1-P1	24.6	1.0	29.5	45.0	2.509	25.58
PB1-P3	23.6	3.0	28.4	45.0	2.479	26.50
PB1-P5	22.7	5.0	27.27	45.0	2.462	27.30
PB2-P1	24.8	1.0	29.7	44.6	2.518	25.50
PB2-P3	24.3 [25.9]	3.0 [3.0]	29.1 [29.0]	43.7 [42.2]	2.507	26.24
PB2-P5	23.8 [25.8]	5.0 [5.0]	28.5 [29.1]	42.8 [40.0]	2.476	27.20
PB3-P1	25.0	1.0	30.0	44.0	2.510	25.59
PB3-P4	25.0	4.0	30.0	41.0	2.485	26.84
PB3-P7	25.0	7.0	30.0	38.0	2.456	28.15
MB0	25.0 [25.1]	—	25.0 [25.0]	50.0 [49.9]	2.531	24.87
MB1-P1	24.5	1.0	24.5	50.0	2.519	25.29
MB1-P3	23.5	3.0	23.5	50.0	2.504	26.05
MB1-P4	23.0	4.0	23.0	50.0	2.490	26.50
MB2-P1	24.8	1.0	24.8	49.5	2.533	25.16
MB2-P3	24.3 [26.0]	3.0 [3.0]	24.3 [23.9]	48.5 [47.1]	2.518	25.94
MB2-P5	23.8 [24.7]	5.0 [5.0]	23.8 [23.9]	47.5 [46.3]	2.488	26.88
MB3-P1	25.0	1.0	25.0	49.0	2.519	25.31
MB3-P3	25.0	3.0	25.0	47.0	2.510	26.05
MB3-P5	25.0	5.0	25.0	45.0	2.487	26.95
PA0	25.0 [25.1]	—	20.0 [20.1]	55.0 [54.8]	2.527	24.72
PA1-P1	24.4	1.0	19.6	55.0	2.501	25.28
PA1-P3	23.3	3.0	18.7	55.0	2.497	25.94
PA2-P1	24.8	1.0	19.8	54.5	2.526	25.04
PA2-P3	24.3 [25.1]	3.0 [3.1]	19.4 [19.3]	53.4 [52.6]	2.513	25.80
PA3-P1	25.0	1.0	20.0	49.0	2.515	25.16
PA3-P3	25.0	3.0	20.0	47.0	2.506	25.91

tendency of P₂O₅ to phase separate/crystallize when introduced into silica-based glasses.^{39,40,45}

- (iv) Although CaO is an important component in bioactive glasses and bioceramics for promoting intracellular and extracellular bodily responses,⁴⁶ CaO-free bioactive glasses and bioceramics displaying bioactivity *in vitro* and *in vivo* have also been proposed in the literature.^{47–54}
- (v) The inclusion of CaO into the glass system would significantly increase the number of experiments. It would be difficult to comprehend all the results and their analysis in one article.

The overarching goal of the study is to develop a comprehensive model elucidating the structure of sodium phospho-borosilicate glasses. Our future studies will focus on understanding the impact of nonframework cation mixing, with special emphasis on elucidating the impact of Ca²⁺ on (i) the short-to-medium-range ordering in the glass structure, and (ii) the kinetics and mechanisms of chemical degradation and ion release from these glasses. The objective of the current and forthcoming articles on this topic is to lay the foundation for a rational design of borosilicate-based bioactive glasses based on the quantitative structure–property relationships (QSPR) approach.

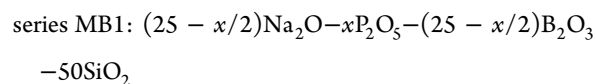
3. EXPERIMENTAL SECTION

3.1. Glass Composition Design. In order to design glasses over a broad compositional space with a variety of structural features, the baseline glasses were selected with respect to their Na₂O/B₂O₃ (=R) ratio. This ratio has been shown to have a significant impact on the short-to-medium-range ordering in the

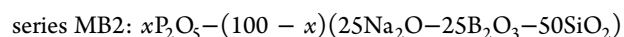
structure of borosilicate glasses as has been shown by Martens and Muller-Warmuth,⁵⁵ and Du and Stebbins.³² Accordingly, three baseline glasses with compositions (mol %) (i) 25 Na₂O–30 B₂O₃–45 SiO₂ (R = 0.83), (ii) 25 Na₂O–25 B₂O₃–50 SiO₂ (R = 1), and (iii) 25 Na₂O–20 B₂O₃–55 SiO₂ (R = 1.25) were selected in the perboric (PB, R < 1), metaboric (MB, R = 1), and peralkaline (PA, R > 1) homogeneous glass-forming regions of the sodium borosilicate ternary diagram.

Further, to unambiguously understand the impact of P₂O₅ on the structure of sodium borosilicate glasses, the former was introduced in the baseline glass systems using three different approaches, with the value of R being constant. The substitution schemes (Schemes 1–3) for metaboric (MB) glasses serve as representative examples for all the glasses investigated in the present study.

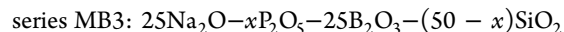
Scheme 1



Scheme 2



Scheme 3



Accordingly, each borosilicate glass system, i.e., perboric (PB), metaboric (MB), and peralkaline (PA), has been further divided into three series of glasses based on the scheme of P₂O₅

substitution and have been labeled in accordance with the above. The batched P_2O_5 contents (x) in the investigated glasses vary between 0 and 9 mol %. However, only the batched compositions resulting in visibly transparent glasses were structurally investigated.

3.2. Glass Synthesis. High purity powders of SiO_2 (Alfa Aesar; 99.5%), H_3BO_3 (Alfa Aesar; $\geq 98\%$), Na_2SiO_3 (Alfa Aesar; $>99\%$), and Na_2HPO_4 (Fisher Chemical; $>99\%$) were used as precursors. Batches corresponding to 70 g of oxides were melted in Pt–Rh crucibles for 1 h in air at temperatures between 1400 and 1500 °C and quenched on a metallic plate. The amorphous nature of glasses was confirmed by X-ray diffraction (XRD) (PANalytical-X'Pert Pro; Cu $K\alpha$ radiation; 2θ range 10–90°; step size $0.01313^\circ s^{-1}$). The glasses were then annealed for 1 h near their glass transition temperatures ($T_g^* - 50^\circ C$, where T_g^* is predicted from the SciGlass database⁵⁶) and slowly cooled to room temperature (see ref 18 for details). Residual stresses of less than 10 MPa were measured using a polariscope. The experimental compositions of the selected glasses (especially those with high Na_2O , B_2O_3 , and P_2O_5 concentration) were analyzed using inductively coupled plasma–optical emission spectroscopy (ICP–OES; PerkinElmer Optima 7300 V) for B_2O_3 , P_2O_5 , and SiO_2 , and flame emission spectroscopy for Na_2O (PerkinElmer Flame Emission Analyst 200). Table 1 presents the compositions of all the glasses investigated in the present study. The density of glasses was measured using Archimedes' method for at least three specimens per glass composition weighed in both air and *d*-limonene.

3.3. Structural Analysis by NMR Spectroscopy. NMR spectra were measured on (i) an Agilent 240-MR DD2 spectrometer (5.7 T) using 3.2, 4.0, and 7.5 mm MAS NMR probes, (ii) Bruker Avance Neo 500 and 600 MHz spectrometers (11.7 and 14.1 T, respectively) using 2.5 and 4.0 mm MAS NMR probes, (iii) an Agilent DD2 system at 16.4 T equipped with a 3.2 mm MAS NMR probe, and (iv) an Agilent VNMRs system at 11.7 T equipped with a 5 mm MAS NMR probe. Table S1 specifies the conditions used for the various single resonance measurements.

One-dimensional refocused INADEQUATE experiments were employed on selected samples to probe the connectivity between phosphate units.⁵⁷ This technique uses double-quantum filtering, based on homonuclear indirect spin–spin (“J-coupling”), for selective detection of P–O–P linked species.⁵⁸ The experiments were performed using a Bruker Avance Neo 600 MHz spectrometer at 14.1 T (243.0 MHz), and a Bruker DSX 500 console interfaced with a 4.7 T magnet, with a 2.5 (4.0) mm probe using a spinning frequency of 15.0 (12.0) kHz, $\pi/2$ pulse lengths near 1.6 (4.0) μs , recycle delays of 5–10 s, and signal averaging over at least 4000 (24000) acquisitions. The double quantum coherence buildup time was set to 16 ms, corresponding to a $^2J(^{31}P-^{31}P)$ coupling constant of 30 Hz.

All the single resonance MAS NMR spectra were analyzed using the DMFit software,⁵⁹ utilizing the Czsimple model for ^{23}Na MAS NMR spectra, Gauss/Lorentz functions for ^{31}P and ^{29}Si MAS NMR spectra, and the “Q MAS 1/2” model and Gauss/Lorentz functions, respectively, for the ^{11}B resonances of 3- and 4-coordinated boron species. N_4 values were determined from the fractional areas of the peaks attributed to the four-coordinated boron species, with a small correction for the overlapping satellite transition of the B(IV) species.⁶⁰

Dipolar interactions between ^{11}B , ^{31}P , and ^{23}Na nuclei were probed using $^{11}B\{^{31}P\}$, $^{23}Na\{^{31}P\}$, and $^{31}P\{^{23}Na\}$ rotational

echo double resonance (REDOR) experiments, in addition to $^{31}P\{^{11}B\}$ rotational echo adiabatic passage double resonance (REAPDOR) spectroscopy, on selected samples. All REDOR experiments involving $^{23}Na-^{31}P$ nuclear interactions were conducted on a Bruker DSX 400 spectrometer using a 4.0 mm probe at 9.4 T. $^{11}B-^{31}P$ double resonance measurements were conducted on a Bruker Avance Neo 600 MHz spectrometer using a 2.5 mm probe at 14.1 T. Table S1 specifies the conditions used for REDOR and REAPDOR experiments. The normalized REDOR and REAPDOR signal intensities $\Delta S = (S_0 - S)/S_0$ (where S and S_0 are the signals (i) with and (ii) without recoupling π pulses, respectively) was plotted as a function of dipolar mixing time (NT_r), where N is the number of rotor cycles and T_r is the rotor period. REDOR experiments were performed using a rotor-synchronized spin echo sequence using π pulses as shown in Table S1. The compensation pulse scheme was used,⁶¹ and π pulses on the ^{31}P channel were phase cycled according to the XY-4 scheme.⁶² Following previously established procedures,^{61,63} dipolar second moments ($M_{2(S-I)}$) (where S represents the observed nucleus and I represents the nonobserved nucleus) were determined by fitting the initial part of the REDOR curves ($\Delta S/S_0 \leq 0.20$) using the parabolic approximation shown in eq 1:⁶¹

$$\frac{\Delta S}{S_0} = \frac{4}{3\pi^2} M_{2(S-I)} (NT_r)^2 \quad (1)$$

The final $M_{2(S-I)}$ values are obtained by calibration with experimental data on the crystalline model compounds BPO_4 and $Na_3P_3O_9$, for which the theoretical second moments can be calculated from crystallographic information.^{64,65} The REAPDOR pulse sequence is typically used in the $S\{I\}$ case where the I -nuclei are quadrupolar, such as ^{11}B , producing more efficient dephasing by applying an adiabatic passage pulse lasting one-third of a rotor period in the middle of the dipolar recoupling period.⁶⁶ As the signal-to-noise ratio of these experiments is limited by the long-spin–lattice relaxation times of the ^{31}P -observe nuclei, data were measured for two or three dipolar mixing times only, using rotor-synchronized π pulses in the ^{31}P channel and an adiabatic passage pulse on the ^{11}B channel. Additionally, a saturation comb of 60 90° pulses ensured a stationary initial magnetization at the beginning of each experiment. Simulated REAPDOR curves for each sample were generated using the SIMPSON program package,⁶⁷ taking into account the experimentally determined spin–spin interaction parameters and the experimental conditions.

3.4. Molecular Dynamics Simulations. Classical molecular dynamics simulations have been employed to obtain further insight into the structure of the glass series PB2, MB2, and PA2, and on the glass PB3-P7, using the batched compositions as reported in Table 1. Models containing about 3500 atoms have been generated (three replicas for each composition) by using the melt-quench approach.⁶⁸ The exact number of atoms and box dimensions are reported in Table S2 for these compositions, as well as for the compositions (mol %): (i) $55Na_2O-45P_2O_5$ and (ii) $40Na_2O-18B_2O_3-42P_2O_5$, which have been similarly modeled for the NMR calculations (described below). The shell model force-fields have been used to describe the interatomic interactions between ionic pairs. In this model, which has been demonstrated to reproduce better the medium-range structure of oxide glasses (especially in terms of T^m distributions and intertetrahedral bond angle distributions),^{69–71} the more polarizable ions (oxygen in this case) are represented by a 355

massive core connected to a massless shell by a harmonic spring. A charge is assigned to both the core and shell. The functional form presented in eq 2, which has been already used in previous studies,⁷² has also been utilized in the present study.

$$U(r_{ij}, r_{c-s}, \theta_{ijk}) = k \frac{q_i q_j}{r_{ij}^2} + A_{ij} e^{-(r_{ij}/\rho_{ij})} - \frac{C_{ij}}{r_{ij}^6} + \frac{1}{2} k_s (r_{core-shell})^2 + \frac{1}{2} k_b (\theta_{ijk} - \theta_{ijk}^0)^2 \exp\left(-\frac{r_{ij}}{\rho} - \frac{r_{jk}}{\rho}\right) \quad (2)$$

Here the first term describes Coulombic interactions between all ions (the core and shell belonging to the same ion are filtered out), the second term is a Buckingham function applied between the cation cores and oxygen shells, and the third term represents the harmonic spring connecting the core and shell of the same oxygen ions whereas the last term is a three-body interaction used to constrain the O–Si–O and O–P–O angles to 109°. All the parameters used are included in Table S3 of the Supporting Information. It is important to highlight that all the parameters have been already used in previous investigations with the exception of the B–O parameter sets.^{20,69,73} The latter have been refined starting from those developed by Edén et al.⁴¹ to be consistent with the other parameters and to better reproduce the N_4 fraction in borosilicate glasses with $[B_2O_3]/[SiO_2] \leq 0.33$. The leapfrog algorithm encoded in the DL_POLY2.14 package⁷⁴ has been used to integrate the equations of motion with a time step of 0.2 fs. The initial configurations were generated by randomly placing the number of atoms in a cubic box, whose dimensions were constrained by the experimental densities. The systems were heated and held at 3200 K for 100 ps in the NVT ensemble ensuring a suitable melting of the samples. The liquids were then cooled to 300 K at a nominal cooling rate of 5 K/ps. The resulting glass structures were subjected to a final equilibration run of 200 ps. Velocity scaling was applied at every step during the quenching of the melt to control the kinetic energy (temperature) of the shells. Coulomb interactions were calculated by the Ewald summation method with a cutoff of 8 Å, whereas short-range cutoff values of 7.5 Å were used for the (vdW) short-range interactions.

3.5. NMR Parameter Calculations. To further guide the interpretation of the NMR experiments, we have also computed the NMR parameters of ^{17}O , ^{31}P , ^{29}Si , ^{11}B , and ^{23}Na nuclei for the PB2-PS, 55Na₂O–45P₂O₅, and 40Na₂O–18 B₂O₃–42P₂O₅ glass compositions. Three models of this glass containing 374 atoms each have been generated as was described above. Magnetic shielding and EFG tensors of the various NFUs present were computed with the NMR-CASTEP⁷⁵ density functional theory (DFT) code using the GIPAW⁷⁶ and PAW⁷⁷ algorithms, respectively. The generalized gradient approximation (GGA) PBE⁷⁸ functional was employed, and the core–valence interactions were described by ultrasoft pseudopotentials generated on the fly. For ^{17}O , the 2s and 2p orbitals were considered as valence states with a core radius of 1.3 Bohr; for ^{29}Si and ^{31}P , a core radius of 1.8 Bohr was used with 3s and 3p valence orbitals; for ^{23}Na , a core radius of 1.3 Bohr was used with 2s, 2p, and 3s valence orbitals, while for ^{11}B , a core radius of 1.405 Bohr was used with 2s and 2p valence states. For the PAW and GIPAW calculations we used two projectors in each s and p angular momentum channel for O and B, and in each s, p, and d channel for Si and Na. Before computing the NMR parameters,

constant volume geometry optimizations of the classically generated models were performed at the Γ point. Wave functions were expanded in plane waves with the kinetic energy cutoff of 610 eV; this has been demonstrated to be long enough to reach converged values for energy and NMR chemical shift.

In this work, to fix the ^{29}Si , ^{11}B , ^{31}P , and ^{23}Na δ scale, the values of 322.1,⁷⁹ 95.05,⁸⁰ 278.8,⁷⁹ and 554.05 ppm⁸¹ have been used for σ_{ref} (in the formula $\delta_{CS}^{iso} = -(\sigma_{sample} - \sigma_{ref})$,⁷⁹ where σ is the magnetic shielding constant). The experimentally determined quadrupolar moments, eQ , of $40.59 \times 10^{-27} \text{ m}^2$ and $104 \times 10^{-27} \text{ m}^2$ were used to calculate quadrupolar coupling constants C_Q for the ^{11}B and ^{23}Na nuclei.⁸² However, since previous works demonstrated that the C_Q values are overestimated using these values, we postscaled the ^{11}B and ^{23}Na C_Q values by the factors 0.842 and 0.46, respectively, as suggested in previous studies.^{80,81} NMR output parameters from CASTEP were analyzed using the SoSNMR software.⁸³

4. RESULTS AND DISCUSSION

4.1. Glass Formation and Bulk Properties. Among the samples within a range of $x = 0$ to 9 mol % for each series, those ultimately selected for study passed the criteria of being transparent in appearance after annealing and showing an amorphous character in XRD (Figure S1). Perboric (Na/B < 1) glasses can incorporate P₂O₅ in amounts up to $x = 5$ –7 mol % while in metaboric and peralkaline glasses the limits are $x = 4$ –5 mol % and $x = 3$ mol %, respectively. Peralkaline glasses synthesized with more than 3 mol % P₂O₅ exhibit evidence of crystalline Na₄P₂O₇ phase formation in XRD—see Figure S1—in addition to being visibly phase-separated/crystallized. ICP-OES (see Table 1) analyses conducted on representative samples show a close agreement of their B₂O₃ and P₂O₅ contents with their batched compositions (within ± 0.6 mol %). The analyzed concentrations of Na₂O and SiO₂ in the baseline glasses are also close to their batched values (within ± 0.5 mol %). However, larger variations in the values of Na₂O and SiO₂ can be seen in P₂O₅-containing glass samples ($x = 3$ –5 mol %), with differences ranging between ± 0.7 and 2.7 mol %. The experimental densities and molar volumes of the synthesized glasses are also presented in Table 1. For the baseline glasses, density values agree with previous trends,⁸⁴ while upon successive introduction of P₂O₅, the molar volume tends to increase, reflecting the larger size of the phosphate component.

4.2. ^{11}B MAS NMR and $^{11}B\{^{31}P\}$ REDOR. Figure 1a–c presents the ^{11}B MAS NMR spectra of glasses in the series PB3, MB3, and PA2 as representatives for all the glasses investigated in the present study. The ^{11}B MAS NMR spectra of all the other glasses have been presented in Figure S2. All the spectra show a structured line shape near 14 ppm, reflecting strong quadrupolar perturbations on the ^{11}B signals of three-coordinated boron, and sharper features near 0 ppm, arising from four-coordinated boron, B(IV), for which quadrupolar interactions are significantly weaker. To obtain satisfactory fits one must assume at least two B(III) and two B(IV) components each (e.g., see Figure 1d and Table S4). While this deconvolution should be considered artificial, it serves well for extracting reliable N_4 values from these spectra. Regarding assignments, we expect B³(III) with three bridging oxygen species within ring and nonring units, but also anionic B²(III) units featuring two bridging and one nonbridging oxygen atoms. For the P₂O₅-free baseline glasses, PB0, MB0, and PA0, the fraction of B(IV) units, N_4 , agrees very well with the previous results on borosilicate glasses, and predictions based on R and the SiO₂/B₂O₃ ($=K$)

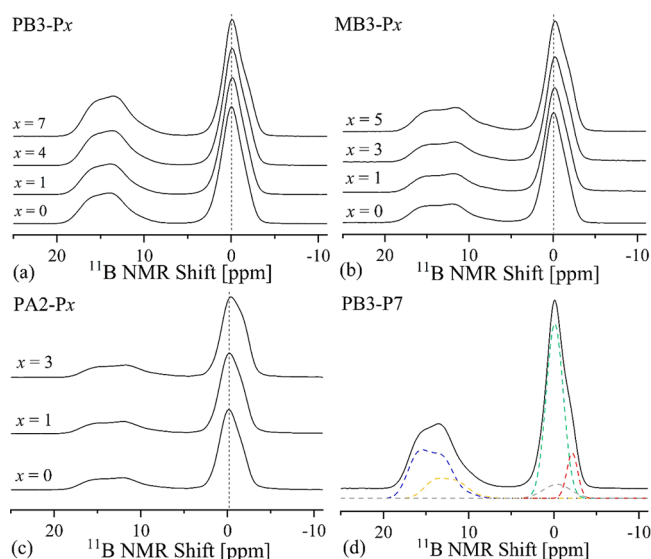


Figure 1. ^{11}B MAS NMR spectra of series (a) PB3, (b) MB3, and (c) PA2 glasses. Series PB3 spectra were collected at 16.4 T while series MB3 and PA2 spectra were collected at 14.1 T. (d) Exemplary line shape deconvolution for the central transition of the ^{11}B MAS NMR spectra of the PB3-P7 glass. Each ^{11}B MAS NMR spectrum was fitted with two Q MAS 1/2 components for the B(III) resonances and three Gauss/Lorentz functions for the B(IV) resonances. The minor fitted peak displayed near 0 ppm represents the central peak of the satellite transition manifold of the B(IV) resonances, which overlaps with the MAS peaks of the central transition, and whose area needs to be considered when extracting N_4 values from these spectra.

Table 2. Calculated Isotropic Chemical Shifts of Boron, Silicon, and Phosphorus NFUs Found in the PB2-P5 Glass Modeled at the MD-GIPAW Level

species	$\delta_{\text{CS}}^{\text{iso}}$ (ppm)	C_Q (MHz)
$\text{P}^1(\text{B(IV)})$	8.2 ± 4.8	—
$\text{P}^1(\text{B(III)})$	7.1 ± 5.1	—
$\text{P}^1(\text{Si})$	4.3 ± 1.8	—
$\text{P}^1(\text{P})$	$3.8 \pm 3.0^{\text{a}}$	—
$\text{P}^2(2\text{B(IV)})$	-3.5 ± 2.6	—
$\text{P}^2(2\text{Si})$	-10.8 ± 3.7	—
$\text{P}^2(\text{SiB(IV)})$	-11.5 ± 1.7	—
$\text{P}^2(\text{B(IV)P})$	$-14.8 \pm 4.4^{\text{b}}$	—
$\text{P}^3(3\text{B(IV)})$	-18.8 ± 3.0	—
$\text{P}^3(\text{Si2B(IV)})$	-23.2 ± 2.0	—
$\text{Si}^4(4\text{B(IV)})$	-82.0 ± 4.1	—
$\text{Si}^4(3\text{B(IV)B(III)})$	-92.0 ± 4.0	—
$\text{Si}^4(\text{SiB(III)2B(IV)})$	-95.5 ± 2.0	—
$\text{Si}^4(2\text{Si2B(IV)})$	-95.9 ± 1.0	—
$\text{Si}^4(2\text{B(IV)2B(III)})$	-98.6 ± 3.0	—
$\text{Si}^4(\text{B(III)B(IV)SiP})$	-99.6 ± 2.5	—
$\text{Si}^4(\text{Si3B(IV)})$	-100.2 ± 4.0	—
$\text{Si}^4(\text{B(IV)3B(III)})$	-100.3 ± 3.5	—
$\text{Si}^4(3\text{SiB(IV)})$	-101.1 ± 3.0	—
$\text{Si}^4(2\text{SiB(IV)B(III)})$	-101.6 ± 1.1	—
$\text{Si}^4(\text{Si2B(III)B(IV)})$	-101.6 ± 3.0	—
$\text{Si}^4(\text{B(IV)2SiP})$	-102.6 ± 2.0	—
$\text{Si}^4(2\text{Si2B(III)})$	-103.2 ± 1.0	—
$\text{Si}^4(4\text{Si})$	-107.2 ± 4.0	—
$\text{Si}^4(4\text{B(III)})$	$-107.6 \pm 2.0^{\text{c}}$	—
$\text{Si}^4(3\text{SiB(III)})$	-109.2 ± 2.0	—
$\text{B}^3(2\text{B(III)Si})$	17.8 ± 0.5	2.85 ± 0.1
$\text{B}^3(3\text{B(IV)})$	17.2 ± 2.0	2.71 ± 0.1
$\text{B}^3(\text{B(IV)B(III)Si})$	16.9 ± 1.8	2.67 ± 0.1
$\text{B}^3(2\text{B(IV)Si})$	16.6 ± 1.3	2.65 ± 0.1
$\text{B}^3(2\text{B(IV)B(III)})$	16.1 ± 1.0	2.68 ± 0.1
$\text{B}^3(2\text{B(IV)P})$	15.9 ± 1.4	2.73 ± 0.1
$\text{B}^3(\text{B(IV)2Si})$	15.1 ± 1.0	2.67 ± 0.1
$\text{B}^3(\text{B(III)2Si})$	14.6 ± 1.6	2.71 ± 0.1
$\text{B}^4(3\text{B(IV)B(III)})$	1.1 ± 0.5	0.26 ± 0.05
$\text{B}^4(\text{B(IV)3B(III)})$	0.6 ± 0.4	0.44 ± 0.05
$\text{B}^4(2\text{B(III)B(IV)Si})$	0.5 ± 0.4	0.60 ± 0.05
$\text{B}^4(3\text{B(IV)Si})$	-0.2 ± 0.3	0.37 ± 0.05
$\text{B}^4(2\text{B(IV)B(III)Si})$	-0.3 ± 0.3	0.41 ± 0.05
$\text{B}^4(4\text{B(III)})$	-0.8 ± 0.4	0.19 ± 0.05
$\text{B}^4(\text{B(IV)3Si})$	-0.8 ± 0.2	0.35 ± 0.05
$\text{B}^4(3\text{B(III)Si})$	-0.9 ± 0.3	0.17 ± 0.05
$\text{B}^4(\text{B(III)3Si})$	-1.0 ± 0.3	0.38 ± 0.05
$\text{B}^4(\text{B}^4\text{B(III)2P})$	-1.5 ± 0.4	0.20 ± 0.05
$\text{B}^4(4\text{Si})$	-2.3 ± 0.4	0.36 ± 0.05

^aAs calculated from MD simulations of a $55\text{Na}_2\text{O}-45\text{P}_2\text{O}_5$ glass ^bAs calculated from MD simulations of a $40\text{Na}_2\text{O}-18\text{B}_2\text{O}_3-42\text{P}_2\text{O}_5$ glass ^cAs calculated from MD simulations of a $25\text{Na}_2\text{O}-56.25\text{B}_2\text{O}_3-18.75\text{SiO}_2$ glass⁷¹

In order to quantify the extent of B–O–P linkages, $^{11}\text{B}\{^{31}\text{P}\}$ REDOR experiments, which probe $^{11}\text{B}-^{31}\text{P}$ magnetic dipole–dipole interactions, have been performed on selected samples. Parts a and b of Figure 2 compare the Fourier transformed ^{11}B MAS NMR spectra in the absence (S_0) and presence (S) of dipolar recoupling and the corresponding difference spectra ($S_0 - S$) for the samples PB3-P7 and MB3-P5, respectively. Such REDOR experiments are instrumental for peak identification

ratio.³⁴ In PB and MB glasses, increasing phosphate content results in a moderate decrease in the fraction of four-coordinated boron, N_4 , which can be attributed to the need for extra charge compensation required for the anionic phosphate species formed. In the case of the PA glasses where significant amounts of $\text{B}^2(\text{III})$ units are expected, the observed invariance of N_4 may be due to the depletion of both anionic four-coordinated B(IV) and anionic three-coordinated $\text{B}^2(\text{III})$ units. The chemical shifts of the $\text{B}^4(\text{IV})$ units, near 0 ppm and -2.5 ppm, are close to those previously reported for $\text{B}^4_{3\text{Si},1\text{B}}$ and $\text{B}^4_{4\text{Si}}$ units, respectively.^{39,85} While the chemical shift near -2.5 ppm may have come from an increased number of Si neighbors around borate units for glasses with $x = 0$, we can alternatively explain it to signify the formation of some B–O–P linkages, which enhances the upfield shoulder somewhat in spectra of glasses containing higher amounts of P_2O_5 . This question has been explored further using chemical shift calculations, MD simulations, and REDOR experiments, as discussed below. Computed isotropic chemical shifts $\delta_{\text{CS}}^{\text{iso}}$ of all $\text{B}^3(\text{III})$ and $\text{B}^4(\text{IV})$ species range between 14 and 18 ppm and between -2.3 and $+1.1$ ppm, respectively, in excellent agreement with the experimental values. Table 2 reveals that the $\delta_{\text{CS}}^{\text{iso}}$ values of both $\text{B}^3(\text{III})$ and $\text{B}^4(\text{IV})$ species are expected to decrease when B(IV) units in the second coordination spheres are replaced by B(III), Si, and/or P. It is also worth noting that in our models, the most negative isotropic chemical shifts of $\text{B}^4(\text{IV})$ are found for species surrounded by either one B(IV), one B(III), and two P atoms (-1.5 ppm), or by four Si NFUs (-2.3 ppm). Thus, on the basis of these calculations, the chemical shift near -2.5 ppm can be ascribed to the formation of either multiple B(IV)–O–Si or of multiple B(IV)–O–P linkages or a combination of both.

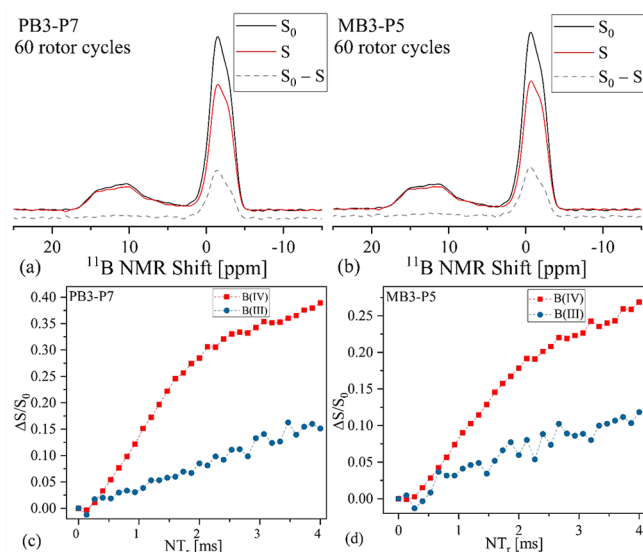


Figure 2. Fourier transforms of the ^{11}B MAS spin echoes obtained in a $^{11}\text{B}\{^{31}\text{P}\}$ REDOR experiment after 60 rotor cycles ($NT_\tau = 4.0$ ms): reference signal, S_0 , signal with dipolar dephasing, S , and REDOR difference spectrum $S_0 - S$, for (a) PB3-P7 glass and (b) MB3-P5 glass. (c and d) $^{11}\text{B}\{^{31}\text{P}\}$ REDOR curves ($\Delta S/S_0$ vs NT_τ) for PB3-P7 and MB3-P5 samples, respectively. Red squares and blue circles denote data points obtained from the dephasing of the B(III) and B(IV) units, respectively.

and assignment based upon spatial proximity (in the present case between ^{11}B and ^{31}P nuclei), detected by reintroducing (recoupling) magnetic dipole–dipole interactions into MAS NMR experiments via coherent pulse trains. This is done by comparing the signal diminution $S_0 - S$ relative to that (S_0) obtained on the sample without recoupling. In the present glasses, heteronuclei occurring within the second coordination sphere from the observed nuclei make the dominant contribution to this diminution. In these experiments, dipolar mixing times of 4.0 ms (60 rotor cycles) have been used. In both samples, the four-coordinated boron species show strong dephasing, while dephasing is significantly weaker for the B(III) units. Based on this finding, we can conclude that only the B(IV) units are involved in B–O–P linkages, whereas B(III) units do not link to phosphate to any significant extent—the slight

dephasing observed here can be easily explained by weaker dipolar interactions with more remote ^{31}P nuclei. Also, parts a and b of Figure 2 indicate that a significant $^{11}\text{B}\{^{31}\text{P}\}$ REDOR effect is observed for both of the B(IV) signal deconvolution components near 0 and -2.5 ppm, signifying B–O–P linking for both of them. For further quantification, we turn to the REDOR curves (plots of $\Delta S/S_0$ versus dipolar mixing times NT_τ , see Figure 2c–d). The initial data regime ($\Delta S/S_0 < 0.2$) has been fitted to eq 1 in order to extract dipolar second moments ($M_{2(\text{B-P})}$) for each sample (see Table 3). Here, the very low $M_{2(\text{B-P})}$ value ($0.1 \times 10^6 \text{ rad}^2/\text{s}^2$) obtained for the B(III) units can be taken as an estimate of a contribution arising from more remote nuclei, which also needs to be accounted for when analyzing the M_2 values measured for the B(IV) units. Accordingly, the corrected M_2 for B(IV) units, $M_{2(\text{B-P})}(\text{B(IV), net})$, is calculated according to the equation $M_{2(\text{B-P})}(\text{B(IV), net}) = M_{2(\text{B-P})}(\text{B(IV)}) - M_{2(\text{B-P})}(\text{B(III)})$, and it is evaluated in terms of the number of B(IV)–O–P linkages. Thus, by directly comparing the $M_{2(\text{B-P})}$ values with that measured for crystalline BPO_4 (four B–O–P linkages at an internuclear distance of 270 pm),²⁸ we can deduce from the information given in Table 3 and Table S4 that the average number of B–O–P linkages per B(IV) species in PB3-P7 is $\langle m_p(\text{B(IV)}) \rangle = 0.37$. Considering the N_4 value, we conclude that, overall, the 60 boron atoms of this glass formulation are involved in 12.5 B–O–P linkages. For the MB3-P5 glass, the average number of B–O–P linkages per B(IV) unit is $\langle m_p(\text{B(IV)}) \rangle = 0.21$; in this case, the 50 boron atoms of the glass formulation make a total of 6.7 B–O–P linkages.

4.3. ^{31}P MAS NMR, Refocused INADEQUATE, $^{31}\text{P}\{^{23}\text{Na}\}$ REDOR, and $^{31}\text{P}\{^{11}\text{B}\}$ REAPDOR. Figure 3 shows the ^{31}P MAS NMR spectra of glasses from series PB2, PB3, MB2, and MB3, while Figure S3 presents the ^{31}P MAS NMR spectra of glasses in the series PB1, MB1, and PA1–PA3. All the ^{31}P line shape parameters and the assignment to the various P^n_{mX} species are summarized in Table S5. The spectra from all the series show three main features: a low intensity peak at ~ 16 ppm (P^0 units), a strong peak centered between 1 and 4 ppm (P^1 units), and a broader feature between -5 and -10 ppm (P^2 units). The chemical shift range associated with the latter suggests a mix of $\text{P}^2_{2\text{B}}$ and $\text{P}^2_{1\text{B},1\text{P}}$ units,³⁹ however, connectivity to Si must also be considered. As the concentration of P_2O_5 increases in the PB and MB series, a decrease in the P^0 signal intensity can be observed, while the intensities of the P^2 species increase monotonically.

Table 3. Dipolar Second Moments ($M_{2(\text{S-I})}$) of Glasses and Model Compounds, As Determined from Parabolic Fits of $S\{I\}$ REDOR Data within $\Delta S/S_0 \leq 0.20$ ^b

sample ID	$M_{2(\text{B-P})} (10^6 \text{ rad}^2/\text{s}^2 (\pm 10\%))$			$\sum r_{(\text{B-P})}^{-6} (10^{60} \text{ m}^{-6})$		$\langle m_p(\text{B(IV)}) \rangle (\pm 10\%)^a$		
	B(III)	B(IV)	B(IV), net	B(III)	B(IV)	$^{11}\text{B}\{^{31}\text{P}\}$ REDOR	^{31}P MAS	$^{31}\text{P}\{^{11}\text{B}\}$ REAPDOR
BPO_4	—	—	20.3 (11.2)	—	0.0105	—	—	—
PB3-P7	0.2 (0.1)	2.0 (1.1)	1.8 (1.0)	0.0001	0.0010	0.37	0.42	0.41
MB3-P5	0.2 (0.1)	1.3 (0.7)	1.1 (0.6)	0.0001	0.0007	0.21	0.26	0.31
sample ID	$M_{2(\text{Na-P})} (10^6 \text{ rad}^2/\text{s}^2)$			$\sum r_{(\text{Na-P})}^{-6} (10^{60} \text{ m}^{-6})$		$M_{2(\text{P-Na})} (10^6 \text{ rad}^2/\text{s}^2)$	$\sum r_{(\text{P-Na})}^{-6} (10^{60} \text{ m}^{-6})$	
$\text{Na}_3\text{P}_3\text{O}_9$	5.4 (3.4)			0.0041		26.7 (8.2)	0.0041	
PB0	—			—		—	—	
PB3-P1	0.3 (0.2)			0.0002		27.8 (8.5)	0.0042	
PB3-P4	1.1 (0.7)			0.0008		24.4 (7.5)	0.0037	
PB3-P7	2.3 (1.4)			0.0018		23.0 (7.0)	0.0035	

^aAverage number of B–O–P linkages per B(IV) unit. ^bHere, S and I denote the observed and the non-observed nuclei. $M_{2(\text{S-I})}$ values in parentheses are raw data before model compound calibration. $M_{2(\text{B-P})}$ data listed for B(IV), net and B(IV), respectively, refer to values with and without correction from the contribution of more remote ^{11}B nuclei to the REDOR curvature. Additionally, calculated values of the average number of P next nearest neighbors around B(IV) were calculated from both double resonance techniques and ^{31}P MAS NMR speciation.

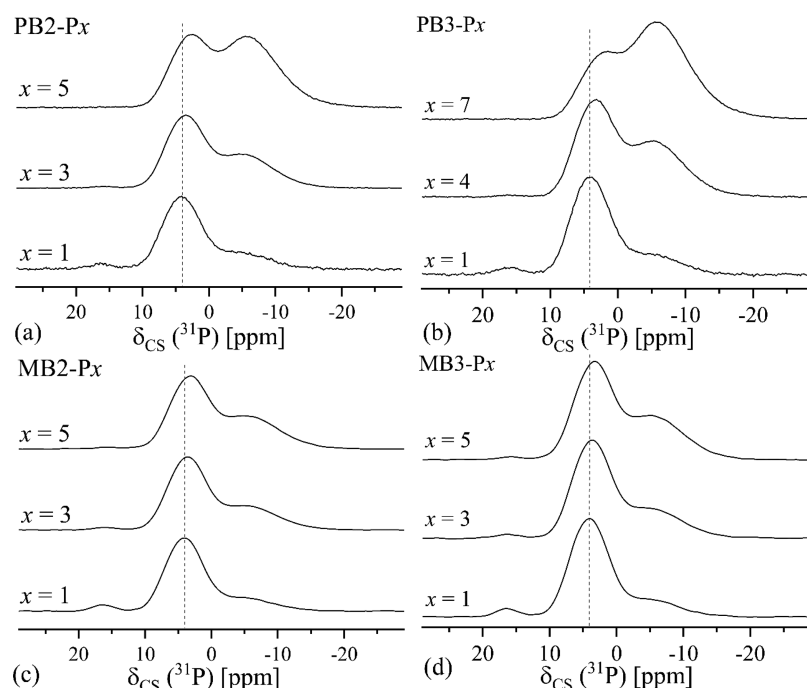


Figure 3. ^{31}P MAS NMR spectra of series (a) PB2, (b) PB3, (c) MB2, and (d) MB3 glasses.

Peralkaline glasses show a slight increase in the intensity of that peak as the concentration of P_2O_5 increases from 1 to 3 mol %, while the changes in the P^0 signal intensity depend upon the substitution scheme used (see Figure S3). The spectra of glasses belonging to the series PA1 show a narrowing of the P^0 and P^1 resonance lines while going from PA1-P1 to PA1-P3 in addition to a low-frequency displacement and increased intensity of the P^0 peak. These changes may indicate the development of more highly ordered phosphate environments. XRD patterns of the $x = 5$ glasses show the formation of crystalline sodium pyrophosphate ($\text{Na}_4\text{P}_2\text{O}_7$), a small amount of which appears to also be present in PA1-P3 glass (see Figure S1 for XRD patterns of PA1-P3 and PA1-P5 samples). Series PA2 and PA3, on the other hand, show similar or slightly decreased P^0 peak intensities from $x = 1$ to 3, alongside small low-frequency shifts in peak position.

Additionally, in glasses of all regimes and series, the P^1 resonance center shifts toward lower frequencies with increasing P content (as displayed in Figure 3). To aid in the assignments of these signals to the various P^n_{mX} units, we have also computed the NMR parameters of the phosphate species found in three replicas of models containing about 400 atoms of the PB2-P5 glass (whose data is reported in Table 2). Additional chemical shift calculations have been performed on phosphate and borophosphate compositions (mol %): $55\text{Na}_2\text{O}-45\text{P}_2\text{O}_5$ and $40\text{Na}_2\text{O}-18\text{B}_2\text{O}_3-42\text{P}_2\text{O}_5$. Our results show that $\text{P}^1_{\text{IB(IV)}}$, P^1_{ISi} , and P^1_{IP} species resonate at about 8.2, 4.3, and 3.8 ppm with standard deviations between 2 and 5 ppm, indicating that these units may not be clearly distinguishable in the broadened MAS NMR spectra. The predicted chemical shifts for the four possible P^2 species, namely $\text{P}^2_{\text{2B(IV)}}$, $\text{P}^2_{\text{1B(IV),1Si}}$, P^2_{2Si} , and $\text{P}^2_{\text{1B(IV),1P}}$, are -3.5 , -11.5 , -10.8 , and -14.8 ppm, respectively, while no value for $\text{P}^2_{\text{1Si,1P}}$ can be found as it has not been generated in the MD simulation of the phospho-borosilicate glass. To further understand the compositional evolution of these spectra, various advanced NMR experiments have been performed to recouple homo- and heteronuclear spin–spin interactions, thereby

providing direct evidence of P–O–P and P–O–B connectivities.

1-D refocused INADEQUATE pulse sequences have been applied to probe the indirect ^{31}P – ^{31}P spin–spin interactions in the samples PB3-P7 and MB3-P5. As this method relies on the existence of through-bond spin–spin interactions to generate double quantum coherences, it can serve as a filter for selectively detecting only those ^{31}P nuclei that are involved in P–O–P linkages. Part a and b of Figure 4 show direct comparisons between the ^{31}P MAS NMR and the INADEQUATE spectra for two selected glass compositions. The double-quantum filtered spectrum of MB3-P5 shows a single component near 2.5 ppm. The same peak is also identified in the INADEQUATE spectrum of the sample PB3-P7. However, an additional component is observed near -10 ppm, whereas the difference spectrum shows components near $+4.6$ and -4.6 ppm. Using the line shape parameters of these partial spectra as additional constraints, the overall ^{31}P MAS NMR spectrum can be fitted to a total of five Gaussian contributions I–V, whose parameters are summarized in Table S5 (see Figure 4). This particular deconvolution model has been used to fit the ^{31}P MAS NMR spectra of all the glasses by maintaining similar Gaussian line widths and positions, allowing the fwhm and $\delta_{\text{CS}}^{\text{iso}}$ to vary within the constraints ± 0.1 ppm and ± 0.5 ppm, respectively. The lone exception to the fitting methodology concerned the PA1-P3 glass composition which, as mentioned previously, exhibited some degree of crystallinity marked by a significant reduction in the fwhm of component II, whose chemical shift agrees with that of pyrophosphate (P^1_{IP}) units. We further note that component II in all samples is narrower than the overall signal near 1 – 4 ppm observed in the single-pulse spectra, requiring the additional components I and III for a satisfactory deconvolution. On the basis of the $^{31}\text{P}\{^{11}\text{B}\}$ REAPDOR results detailed below, component I is tentatively assigned to P^1_{IB} units. For component III, the possibilities include P^1_{Si} and P^2_{2B} .

Further insight into this question comes from $^{31}\text{P}\{^{11}\text{B}\}$ REAPDOR experiments. Parts a and b of Figure 5 show the

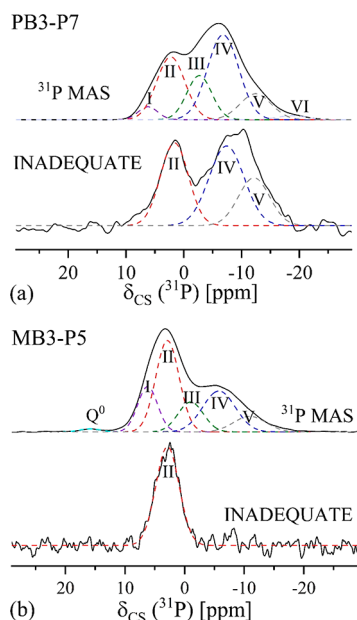


Figure 4. Deconvolution of the ^{31}P MAS NMR and double-quantum filtered ^{31}P MAS NMR spectra, using the refocused INADEQUATE sequence: (a) PB3-P7 and (b) MB3-P5 samples. The double-quantum filtered spectra were utilized to guide the fitting of ^{31}P MAS NMR spectra. Red, blue, and green data points represent the full spectra, the filtered spectra, and the difference spectra, respectively.

displayed are the difference spectra ($S_0 - S$), which indicate that the phosphate species contributing to both major resonances near 1–4 ppm and –5 to –10 ppm show significant ^{11}B – ^{31}P dipole–dipole coupling. We conclude that these phosphate species have, at least in part, ^{11}B next nearest neighbors. Two and three points on the REAPDOR curve have been measured for MB3-P5 and PB3-P7, respectively, and they are compared with data generated from SIMPSON simulations taking into account the natural abundance of the ^{11}B isotope (80.4%) (see Figure 5c,d). In these simulations, the P–B distance across a P–O–B linkage has been assumed to be 270 pm, consistent with the shortest distance in BPO_4 .⁶⁴ Simulations are based on a ^{11}B quadrupolar coupling constant of 0.52 and 0.64 MHz for glasses MB3-P5 and PB3-P7, respectively. These values have been taken from the overall spectral range of the spinning sideband pattern associated with the $|m| = 1/2 \leftrightarrow |m| = 3/2$ satellite transitions (see Figure S4). For spin- $3/2$ nuclei, this overall spectral range is identical with the quadrupolar coupling constant, C_Q . We can see from the simulations that the signal near –5 to –10 ppm shows a stronger REAPDOR effect compared to that simulated for a single P–O–B linkage (about 1.1 and 1.2 per P unit in PB3-P7 and MB3-P5), whereas the signal in the 1 to 4 ppm range shows a weaker interaction (about 0.65 and 0.8 P–O–B linkages per P unit). While the P^0 peak also shows evidence of some weak dephasing in the MB3-P5 sample, this effect must be attributed to contributions from more remote ^{11}B nuclei in the glass.

In light of the above-discussed results, the most likely candidates for structural species detected in our experiments, based upon the studied compositional regime and the experimental ^{31}P chemical shifts, are $\text{P}^1_{\text{IB(IV)}}$ (component I),

Fourier transforms of rotor-synchronized ^{31}P spin echoes without (S_0) and with (S) ^{11}B dipolar recoupling for the samples PB3-P7 and MB3-P5 after 16 and 22 rotor cycles. Also

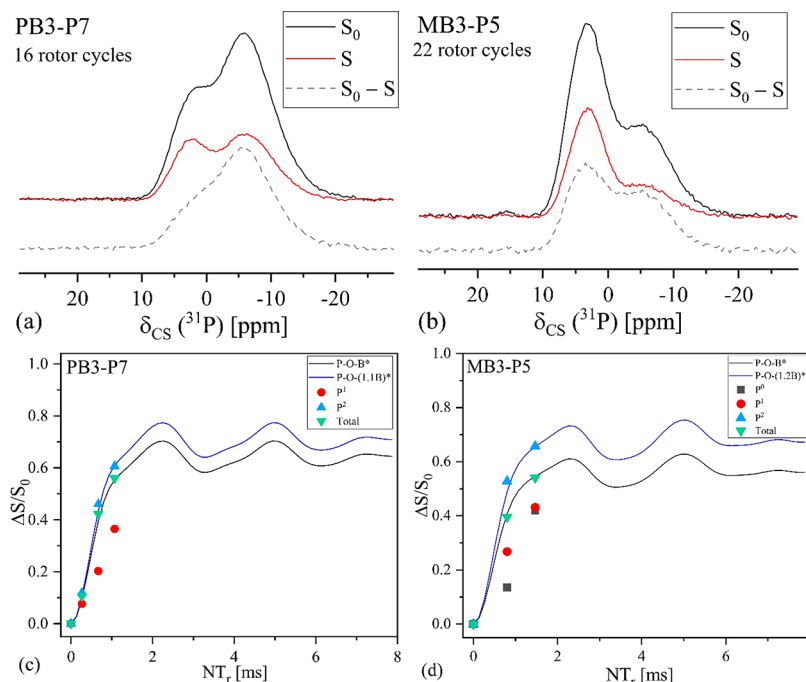


Figure 5. Fourier transforms of the ^{31}P MAS spin echoes obtained in a $^{31}\text{P}\{^{11}\text{B}\}$ REAPDOR experiment: reference signal, S_0 , signal with dipolar dephasing, and REAPDOR difference spectra $S_0 - S$. Key: (a) PB3-P7 glass after 16 rotor cycles ($NT_r = 1.1$ ms) and (b) MB3-P5 glass after 22 rotor cycles ($NT_r = 1.5$ ms). (c and d) $^{31}\text{P}\{^{11}\text{B}\}$ REAPDOR curves ($\Delta S/S_0$ vs NT_r) for PB3-P7 and MB3-P5 samples, respectively, for the resolved resonances of P^0 , P^1 , and P^2 units and the integral, after a given evolution time. The solid lines represent the results from numerical simulations made with the SIMPSON software. The black curve represents the REAPDOR curves for a ^{11}B – ^{31}P two-spin system assuming an internuclear distance equal to that of a P–O–B linkage found in BPO_4 (270 pm). The blue curve has been scaled to the experimental data of the P^2 species in order to deduce an average number of P–O–B linkages.

Table 4. Average Number of B Next Nearest Neighbors around P and Average Number of Bridging Oxygen Atoms per Phosphate Unit As Determined from Fitted ^{31}P MAS NMR Data^c

sample ID	^{31}P MAS NMR		^{29}Si MAS NMR		^{23}Na MAS NMR	
	$\langle n_{\text{B}}(\text{P}) \rangle$	$\langle n \rangle$	$\text{Si}^4(\text{calcd})$	δ_{cg}	$\delta_{\text{CS}}^{\text{iso}}$ (ppm)	C_{Q} (MHz)
PB0	—	—	70.8	−91.9	−5.2	2.4
PB1-P1	0.50	1.28	83.4	n.d. ^b	−5.2	2.5
PB1-P3	0.73	1.56	92.0	n.d.	−5.8	2.5
PB1-P5	0.91	1.77	97.7	n.d.	−5.4	2.6
PB2-P1	0.47	1.23	81.5	n.d.	−5.3	2.4
PB2-P3	0.65	1.45	84.5	n.d.	−5.0	2.6
PB2-P5	0.90	1.74	88.3	n.d.	−5.7	2.5
PB3-P1	0.48	1.24	80.8	−92.3	−5.9	2.2
PB3-P4	0.73	1.50	95.1	−95.3	−6.5	2.2
PB3-P7	1.02/1.20 ^a	1.83/1.86 ^a	100.3	−99.7	−6.4	2.2
MB0	—	—	66.7	−92.1	−3.0	2.7
MB1-P1	0.72	1.29	77.4	−93.0	−6.4	2.9
MB1-P3	0.84	1.50	88.1	−96.2	−7.9	2.8
MB1-P4	0.88	1.56	91.4	−97.5	−8.8	2.8
MB2-P1	0.69	1.25	74.6	−92.5	−6.0	2.9
MB2-P3	0.81	1.45	77.8	−95.2	−7.8	2.8
MB2-P5	0.86	1.56	92.1	−97.4	−9.0	2.7
MB3-P1	0.69	1.24	74.1	−91.9	−5.8	2.8
MB3-P3	0.80	1.42	85.1	−94.1	−7.3	2.8
MB3-P5	0.84	1.55	92.3	−96.7	−9.0	2.7
PA0	—	—	61.7	−91.3	−4.8	2.9
PA1-P1	0.61	1.21	68.9	−94.6	−6.7	2.8
PA1-P3	0.62	1.30	84.0	−96.4	−6.8	2.8
PA2-P1	0.67	1.24	68.3	−92.8	−5.1	2.9
PA2-P3	0.74	1.39	77.3	−95.2	−7.0	2.8
PA3-P1	0.66	1.21	66.6	−92.7	−5.0	2.9
PA3-P3	0.71	1.33	77.8	−95.1	−6.2	2.8

^aTwo separate sets of measurements with fits constrained by refocused INADEQUATE experiments. ^bNot determined. ^c ^{29}Si chemical shifts δ_{cg} (center of gravity, ± 0.5 ppm), calculated Si^4 fractions ($\pm 1.0\%$) based on charge balance, average ^{23}Na isotropic chemical shifts, $\delta_{\text{CS}}^{\text{iso}}$ (± 0.5 ppm), and quadrupolar coupling constants C_{Q} (± 0.2 MHz).

P^1_{IP} (component II), and P^2_{2B} (component III). Additionally, P^1_{1Si} species may contribute to component II or III, which in the latter case would have the effect of weakening the overall REAPDOR response. Plausible assignments for component IV and V are the species $\text{P}^2_{\text{1B,1P}}$ and $\text{P}^3_{\text{2B,1P}}$ as these signals appear both in the refocused INADEQUATE experiments and in the REAPDOR difference spectra.³⁸ In addition, subtle differences arising from a detailed comparison of the refocused INADEQUATE spectra and the REAPDOR difference spectra suggest that the P^1_{1Si} and $\text{P}^2_{\text{1B,1Si}}$ units may be present as well, the former contributing intensity mostly to signals III and IV and latter contributing intensity mostly to signal V in the sample PB3-P7. Concerning the sample MB3-P5, we further believe that the resonances associated with $\text{P}^2_{\text{1B,1P}}$ and $\text{P}^3_{\text{2B,1P}}$ units may have eluded the double-quantum filtered detection in Figure 4b due to their low concentrations. Minor components labeled P^0 and VI are attributed to isolated monophosphate (P^0) or P^2_{2P} chain phosphate species which do not contain any linkages to boron. Table S5 presents the proposed phosphate speciation of all the samples as determined from the spectral deconvolutions. In the case of sample PB3-P7, two separate sets of analyses including refocused INADEQUATE experiments have been performed; the deviations give an impression of the possible experimental error in the speciation.

The data presented in Table S5 reveals some universal trends, regardless of R regime: As x increases from 1 to higher values, the concentrations of P^0 and P^1 species decrease monotonically,

while those of P^2 and P^3 increase. The concomitant increase in connectivity can be expressed by the average number of bridging oxygen atoms per phosphate unit given by eq 3 and presented in Table 4.

$$\langle n \rangle = 0 \times f(\text{P}^0) + 1 \times f(\text{P}^1) + 2 \times f(\text{P}^2) + 3 \times f(\text{P}^3) \quad (3)$$

Furthermore, for all the glass compositions investigated in the present study, a general rise in $\text{P}-\text{O}-\text{B}$ linked phosphate units has been observed with increased P_2O_5 presence in the glass network, with a preference toward units that have at least two bridging oxygen atoms (P^2 units). While there is a decrease in the concentration of P^1_{1B} units, those of other B linked P^2 units (P^2_{2B} , $\text{P}^2_{\text{1B,1Si}}$, $\text{P}^2_{\text{1B,1P}}$) and some $\text{P}^3_{\text{2B,1P}}$ units as well become more prominent, with the average number of B next nearest neighbors for each P in the glass rising from 0.5 to 0.9–1.2 in PB glasses, rising from 0.7 to 0.8–0.9 in MB glasses, and either remaining similar or rising from 0.6 to 0.7 in PA glasses (Table 4). These values have been calculated from the P^n_{mB} concentrations, according to the assessed speciation from ^{31}P MAS NMR. While in glasses with $x = 1$ about half (40–60%) of the phosphate units have no linkages to boron (i.e., are either P^0 or P^1_{1P}), higher concentrations of P_2O_5 are linked more extensively with B, as they contain higher levels of P^2 units. This effect is most pronounced in the perboric (PB) glass having the highest P_2O_5 content (e.g., PB3-P7).

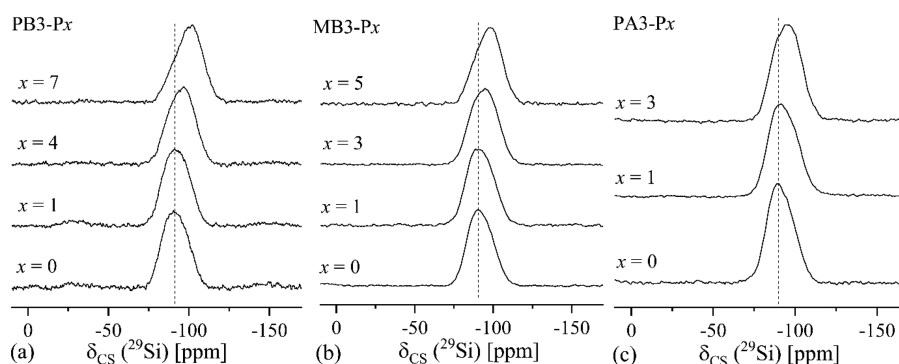


Figure 6. ^{29}Si MAS NMR spectra of series (a) PB3, (b) MB3, and (c) PA3 glasses. The dashed lines are guides to the eye.

To validate our results, we can compare the average dipolar interaction strengths measured in the $^{11}\text{B}\{^{31}\text{P}\}$ REDOR and the $^{31}\text{P}\{^{11}\text{B}\}$ REAPDOR experiments—both techniques should give consistent results, i.e., the total number of B–O–P linkages as determined from ^{11}B NMR should equal the total number of P–O–B linkages derived from ^{31}P NMR. From the $^{11}\text{B}\{^{31}\text{P}\}$ REDOR experiments, which yield the average number of B–O–P linkages per B(IV) unit from the second moment $M_2(\text{B–P})$, the total number of B–O–P linkages is given by eq 4, neglecting any B(III)–O–P linkages in the network.

$$\#(\text{B–O–P}) = N_4 \times 2 \times \text{mol. \%B}_2\text{O}_3 \times \langle m_{\text{P}}(\text{B}) \rangle \quad (4)$$

As detailed above, 60 boron atoms in glass PB3-P7 make a total of 12.5 B–O–P linkages whereas the 50 boron atoms in glass MB3-P5 make a total of 6.7 B–O–P linkages.

For comparison, the average number of B–O–P linkages per P can be deduced from the simulation of the REAPDOR dephasing observed for the total integrated ^{31}P MAS NMR signal (see Figure S, parts a and b). As shown in Figure S-c-d, this number is found near $\langle n_{\text{B}}(\text{P}) \rangle = 1.0$ for both samples. Thus, the total number of P–O–B linkages is given by $\#(\text{P–O–B}) = 2x\langle n_{\text{B}}(\text{P}) \rangle$. For example, the 14 phosphorus atoms in glass PB3-P7 make a total of 14 P–O–B linkages whereas the 10 phosphorus atoms in glass MB3-P5 make a total of 10 P–O–B linkages. Yet another independent estimate of $\#(\text{P–O–B})$ is available from the phosphorus speciation as listed in Table S5. From the calculated values $\langle n_{\text{B}}(\text{P}) \rangle$ shown in Table 4, we conclude that there are 14.3/16.8 and 8.6 P–O–B linkages in samples PB3-P7 (measured twice) and MB3-P5, respectively, in good agreement with the REAPDOR estimate. This consistency also confirms our ^{31}P MAS NMR peak assignments within the entire body of NMR data collected. Table 3 displays these comparisons for the two studied samples, expressing the results in terms of the average number of B–O–P linkages per B(IV) unit, as calculated from the phosphorus speciation according to eq 5.

$$\begin{aligned} & \frac{\text{avg. \#B–O–P linkages}}{\text{B(IV)}} \\ &= \frac{(\text{avg. \#B per P}) \times (\text{P content, mol. \%})}{(N_4 \text{ fraction}) \times (\text{B content, mol. \%})} \end{aligned} \quad (5)$$

All the results have been summarized in Table 4. The data presented in Table 4 further shows that the rate of change of $\langle n_{\text{B}}(\text{P}) \rangle$ as a function of x increases in the order PA → MB → PB, as does the number of P–O–B linkages formed for a fixed x -value. Thus, the more highly polymerized PB glasses tend to mix more extensively with P than the MB or PA glasses as the P_2O_5

content is increased. However, due to the well-known affinity of phosphate units toward sodium, the extent of P–O–B mixing is also highly dependent upon the Na^+ distribution in the network. Alternatively, the affinity of glasses to form P–O–B(IV) linkages can also greatly affect Na^+ distribution among NFUs, as the average bond valence of tetrahedral phosphate and boron units balance $\left(\frac{1.25 + 0.75}{2} = 1\right)$,⁸⁶ indicative of high bond stability and presumptive charge-sharing between negatively charged B(IV) units and nonbridging oxygen on phosphate species.^{87,88} These competing factors will be further discussed in the next sections.

4.4. ^{29}Si MAS NMR. Figures 6 and S5 present the ^{29}Si MAS NMR spectra of samples in the series MB3, PB3, and PA3 as well as MB1, MB2, PA1, and PA2 samples. Each series displays a broad peak centered near -92 ppm in the phosphate-free glass which shifts significantly toward lower frequency with increased P_2O_5 content. A similar trend has also been observed by Muñoz et al.³⁹ in a compositionally related borosilicate system. The signal positions we see in our samples are also consistent with previously studied P_2O_5 -free and P_2O_5 -containing alkali borosilicate glasses of similar R and K ($= [\text{SiO}_2]/[\text{B}_2\text{O}_3]$) values.^{39,89,90} Owing to the poor resolution, no unambiguous line shape deconvolution is possible here. Therefore, Table 4 lists the average ^{29}Si chemical shifts determined from the center of gravity. We clearly note that this quantity shifts significantly toward lower frequency with increasing P_2O_5 content. As the ^{29}Si chemical shifts in compositionally complex mixed-network former glasses are influenced by numerous different factors, including the number of NBOs and the number of next nearest neighbor linkages the trend observed here can be explained in different ways. Further guidance comes from quantum chemical calculations of chemical shifts done on PB2-P5 glass, which are summarized in Table 2 for various Si^4 species with different connectivities. The calculations confirm the trends found by Fortino et al.⁷¹ While $\delta_{\text{CS}}^{\text{iso}}(^{29}\text{Si})$ increases when Si atoms are replaced by borate species in the second coordination sphere, the effect is significantly stronger for Si–O–B(IV) linkages than for Si–O–B(III) linkages. For example, the computed isotropic chemical shift for a $\text{Si}^4_{4\text{B(IV)}}$ species is -82.0 ppm while it is -107.6 ppm for a $\text{Si}^4_{4\text{B(III)}}$ species⁷¹ (see Table 2). Intermediate values are found for Si^4 species with mixed B(III), B(IV), and Si^4 ligation. The chemical shift ranges of such species overlap with those usually associated with Si^2 and Si^3 units in silicate glasses, making a corresponding assignment difficult. The situation is complicated further if ligation to phosphorus is considered, as replacement of a Si–O–Si linkage by a Si–O–P linkage produces a shift that is more negative than that of $\text{Si}^4_{4\text{Si}}$. Given

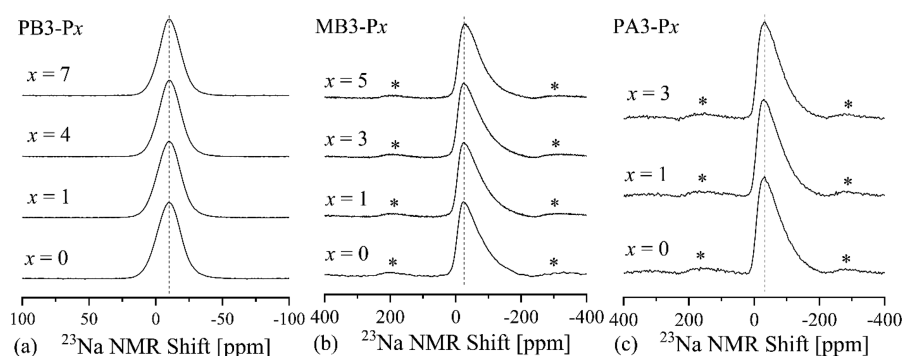


Figure 7. ^{23}Na MAS NMR spectra of series (a) PB3, (b) MB3, and (c) PA3 glasses. Series PB3 spectra were collected at 16.4 T while series MB3 and PA3 spectra were collected at 5.7 T. The asterisks mark spinning sidebands and the dashed lines serve as guides to the eye.

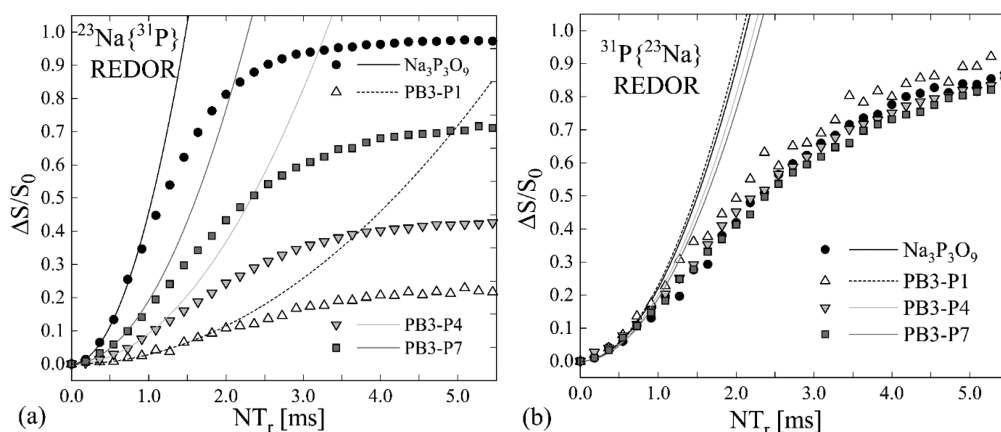


Figure 8. (a) $^{23}\text{Na}\{^{31}\text{P}\}$ and (b) $^{31}\text{P}\{^{23}\text{Na}\}$ REDOR curves for the model compound $\text{Na}_3\text{P}_3\text{O}_9$ and the glass samples PB0, PB3-P1, PB3-P4, and PB3-P7. The solid curves represent parabolic fits to the initial regime ($\Delta S/S_0 \leq 0.20$) from which the heteronuclear second moments are extracted via eq 1.

this situation and the poorly resolved lineshapes, it is not possible to deduce detailed silicon speciation from the ^{29}Si MAS NMR spectra alone. Si^4 species connected to a mix of Si, B(III), and B(IV) are likely to be present; in addition, there may be some contribution from Si^3 units. In similar sodium phospho-borosilicate glasses, Muñoz et al.³⁹ attributed the ^{29}Si chemical shift trend observed upon the addition of P_2O_5 to a decrease in silicate-borate network connectivity. However, it might also reflect a diminution of Si^3 units or, in principle, an increase in the number of Si–O–P linkages. From the charge balance constraint (eq 6),

$$[\text{Si}^3] + [\text{B(IV)}] + [\text{P}^2] + 2[\text{P}^1] = [\text{Na}] \quad (6)$$

we can deduce the concentration of Si^3 units if we neglect the $\text{B}^2(\text{III})$ units. These numbers, listed in Table 4, show that the addition of phosphate in these glasses tends to diminish $[\text{Si}^3]$, i.e., the concentration of NBOs in the silicate network. Again this effect can be attributed to the successful competition of P_2O_5 over SiO_2 in attracting network modifier and/or effective charge-sharing between P and B units in P–O–B(IV) linkages in the absence of network modifying species.

4.5. ^{23}Na MAS NMR and $^{23}\text{Na}\{^{31}\text{P}\}$ and $^{31}\text{P}\{^{23}\text{Na}\}$ REDOR. Figure 7a–c presents the ^{23}Na MAS NMR spectra of series MB3, PB3, and PA3. The differences in appearance are attributed to the different magnetic field strengths used for data collection. The spectra for MB and PA samples have been collected at 5.7 T, while PB samples have been measured at 16.4 T. Therefore, the extent of second-order quadrupolar broadening is very different for the low and high field data. The ^{23}Na

isotropic chemical shift ($\delta_{\text{CS}}^{\text{iso}}$) and C_Q values listed in Table 4 have been extracted from the fitted spectra using the Cjzek distribution model implemented in DMfit. The isotropic chemical shift values in MB glasses show a monotonic decrease from near -3 to -9 ppm with increasing x , while PB and PA glasses show much less pronounced effects. The isotropic chemical shift is expected to be highly dependent upon the distribution of sodium among the silicate, borate, and phosphate structural units, whose anionic charges it compensates. On the basis of the findings of the present study, the main change as a function of x in all three series is the increased participation of phosphate in the anionic inventory of the glass. The overall ^{23}Na chemical shift trend toward more negative values with increasing x reflects the increased importance of sodium/phosphate interactions, and the simultaneous decrease of the importance of B(IV)–Na and Si^3 –Na interactions.

Further, to probe Na–P interactions in the glass network, $^{23}\text{Na}\{^{31}\text{P}\}$, and $^{31}\text{P}\{^{23}\text{Na}\}$ dipole–dipole couplings have been measured in the glasses and the crystalline model compound $\text{Na}_3\text{P}_3\text{O}_9$ for calibration. Again, M_2 values have been extracted via eq 1 from the initial portion of each REDOR curve ($\Delta S/S_0 < 0.2$; see Figure 8), and are presented in Table 3. As anticipated, $M_2(\text{Na–P})$ increases with increasing x . We estimate the average coordination of the sodium ions with phosphorus in the second coordination sphere at 0.3, 1.0, and 2.1 P for samples PB3-P1, PB3-P4, and PB3-P7, respectively. This trend in ^{23}Na – ^{31}P proximity is accompanied by decreases in the Si^3 and N_4 fractions (see Tables 4 and S4), suggesting that Na^+ ions, which in the phosphate-free borosilicate glasses either charge

Table 5. N_4 Values and Fractions of $B^4(IV)$, $B^3(IV)$, $B^3(III)$, and $B^2(III)$ Units Found in the MD-Generated Structural Models of the Investigated Glasses and Average Numbers of Network Former Cations Bound to Fully Connected $B^4(IV)$ and $B^3(III)$ Units^a

sample ID	N_4	$B^3(IV)$	$B^4(IV)$	#B(IV)	#B(III)	#Si	#P	#P (³¹ P MAS NMR)
PB0	59.5 [62.9]	2.0	57.5	1.0	1.0	2.0	—	—
PB2-P1	60.5 [63.5]	1.6	58.9	0.9	1.0	2.1	0.0	0.0
PB2-P3	58.6 [62.1]	1.8	56.8	0.9	1.1	1.9	0.2	0.1
PB2-P5	54.6 [59.1]	1.3	53.3	0.7	1.1	1.9	0.3	0.3
PB3-P7	53.8 [56.4]	3.9	49.9	0.7	1.1	1.7	0.5	0.4
MB0	61.7 [67.2]	4.4	57.3	0.9	0.8	2.3	—	—
MB2-P1	63.4 [67.5]	3.4	60.0	1.0	0.9	2.1	0.0	0.0
MB2-P3	60.9 [67.2]	2.7	58.2	0.8	0.9	2.2	0.2	0.2
MB2-P5	60.3 [65.5]	2.2	58.1	0.7	0.9	2.2	0.3	0.3
PA0	67.2 [71.0]	5.8	61.4	0.8	0.6	2.7	—	—
PA2-P1	58.9 [71.4]	2.1	56.8	0.6	0.8	2.5	0.0	0.0
PA2-P3	66.6 [71.9]	3.4	63.2	0.8	0.6	2.5	0.2	0.2
Sample ID	N_3	$B^2(III)$	$B^3(III)$	#B(IV)	#B(III)	#Si	#P	
PB0	40.5	9.9	30.6	1.7	0.3	1.0	—	
PB2-P1	39.5	6.7	32.8	1.6	0.4	1.0	0.0	
PB2-P3	41.4	4.1	37.3	1.7	0.3	1.1	0.0	
PB2-P5	45.4	4.5	40.9	1.5	0.4	1.1	0.0	
PB3-P7	46.2	1.7	44.5	1.5	0.5	1.0	0.0	
MB0	38.3	12.5	25.8	1.6	0.3	1.1	—	
MB2-P1	36.6	7.5	29.1	1.6	0.2	1.2	0.0	
MB2-P3	39.1	7.4	31.7	1.5	0.3	1.2	0.0	
MB2-P5	39.7	4.7	35.0	1.4	0.3	1.2	0.1	
PA0	32.8	13.9	18.9	1.5	0.1	1.4	—	
PA2-P1	41.1	10.0	31.1	1.4	0.2	1.4	0.0	
PA2-P3	33.4	8.6	24.8	1.4	0.2	1.4	0.0	

^a# indicates the average number of linkages from $B^4(IV)$ and $B^3(III)$ species to each NFU. N_4 values measured by NMR are listed in brackets. #P neighbors around $B^4(IV)$ have also been compared to the values as calculated from fitting of ³¹P MAS NMR data.

compensate $B(IV)$ units or create NBOs in the silicate network, are now more closely associated with phosphate units. Consistent with this interpretation, the $M_{2(P-Na)}$ values measured in the reverse ³¹P{²³Na} REDOR experiments remain roughly constant as a function of x , suggesting a rather constant environment of the phosphate units with sodium ions.

4.6. MD Simulations: Glass Structure Predictions. MD simulations have been performed on one series per Na/B regime (series PB2, MB2, and PA2; including the P_2O_5 -free counterparts) in order to (i) compare and prove the validity of using MD simulations to reproduce and predict glass structures and (ii) obtain additional structural details that are not readily available from MAS NMR.

Boron Environment: Short-Range Order. Reliable B–O interatomic parameters must first be validated by their ability to accurately reproduce the N_4 values as a function of composition. In this respect, Table 5 indicates good agreement between simulated and experimental data. For each series investigated, the majority of the boron atoms are four-coordinated ($N_4 > 0.53$), although the experimental N_4 values are always higher by 5–7% compared to the simulated data. Nevertheless, the simulations reflect the same trends observed experimentally: N_4 tends to decrease in the order PA → MB → PB and with increasing P_2O_5 content. Table 5 further indicates that the large majority (>91%) of the four-coordinated boron species $B(IV)$ are bound to four bridging oxygen atoms, i.e., they are $B^4(IV)$ species. The fraction of $B(IV)$ species linked to NBOs, denoted $B^3(IV)$ species, is negligible. It should be noted here that this kind of information is not available from solid-state NMR, as the NMR-parameters of four-coordinated boron atoms bound to

NBOs are unknown and the spectra of both species are most likely overlapping.

The same kind of analysis has also been conducted on the three-coordinated boron ($B(III)$) species. Table 5 reveals that the majority of them are $B^3(III)$ species (trigonal B unit with three BO), but the simulations also suggest that there are non-negligible amounts of $B^2(III)$ units bearing one nonbridging oxygen. In this context, it is important to note that small concentrations of $B^2(III)$ units are difficult to detect and quantify by high-field ¹¹B MAS NMR, and the low-field data by Yun and Bray based on their detailed analysis of ¹¹B and ¹⁰B wide-line NMR spectra³³ remain the best estimates known to date. In line with these wide-line NMR results, the MD simulations indicate that the fraction of $B^2(III)$ units decreases with decreasing R values, i.e., in the order PA → MB → PB. Furthermore, in agreement with these general trends, Table 5 reveals that the successive incorporation of P_2O_5 into these glasses has the effect of depleting the $B^2(III)$ units drastically. Such information is currently not available experimentally from the ¹¹B NMR data presented here, even when analyzing boron speciation with ¹¹B 3QMAS NMR spectroscopy (data not shown).

Boron Environment: Connectivity. Table 5 lists the average number of each NFU around each $B^4(IV)$ and $B^3(III)$ unit, as extracted from the MD generated models. In general, $B^4(IV)$ species are connected to 1.9–2.3 Si atoms and nearly equal amounts (between 0.7 and 1.1) of $B(III)$ and $B(IV)$ species in the PB2 and MB2 series. In both series, the number of P atoms connected to $B^4(IV)$ species increases (up to 0.3 per $B^4(IV)$ species) with the addition of P_2O_5 . While the experimental data from NMR do not permit such an incisive numerical analysis, we

can compare the simulated average number of B(IV)–O–P linkages per boron with the results from $^{11}\text{B}\{^{31}\text{P}\}$ REDOR. For the glass PB3-P7, we note an excellent quantitative agreement. Also, the MD simulations agree with the experimental REDOR result that there are very few if any B(III)–O–P linkages. Interestingly, we also see that P prefers to replace B(IV) and Si as opposed to B(III) species in the second coordination sphere of $\text{B}^4(\text{IV})$. In the PA2 series, the second coordination sphere of $\text{B}^4(\text{IV})$ has more Si atoms (2.5–2.7) and fewer B(IV) and B(III) units (0.6–0.8) compared to the PB2 and MB2 series. In this case, P seems to preferentially replace Si instead of B(IV). Again, such detailed information is not currently available from solid-state NMR.

Overall, the MD simulations confirm the NMR result that phosphorus promotes a restructuring of the borate component. $\text{B}^4(\text{IV})$ species are mainly surrounded by silicon atoms and phosphate units, whereas $\text{B}^3(\text{III})$ species are mainly connected to B(IV) species (between 1.4 and 1.7), silicon (1.0–1.4), and to a very small extent, other B(III) species (0.1–0.4). Unlike B(IV) species, B(III) species tend to avoid linking to phosphorus. While the MD simulations suggest that the fraction of B(III)–O–Si linkages tends to increase with x , no such information can be drawn from the NMR data, as they do not reveal any discernible spectroscopic trends for the B(III) units.

The effect of the network former mixing in the second coordination sphere of the boron atoms was thoroughly investigated in a previous theoretical study on $25\text{Na}_2\text{O}-x\text{B}_2\text{O}_3-(75-x)\text{SiO}_2$ ($x = 0-75$ mol %) glasses.⁷¹ That work showed that (i) the positions and areas of the B(III) and B(IV) peaks in the ^{11}B MAS NMR spectra of the simulated glasses are in good agreement with their experimental counterparts, which validates the accuracy of the structural models and NMR calculations, (ii) the ^{11}B isotropic chemical shift decreases with the B–O–T angle and with the amount of silicon in the second coordination sphere of boron, and (iii) the substitution of B(III)/B(IV)–O–B(III) bonds by B(III)/B(IV)–O–B(IV) bonds leads to an increase in the isotropic chemical shift. Unfortunately, the $^{11}\text{B}(\text{III})$ NMR parameter analyses are not sufficiently distinctive to monitor the changes in the second coordination sphere of these units as P_2O_5 is added to these glasses. This may be possible, however, by $^{11}\text{B}\{^{29}\text{Si}\}$ REDOR experiments to be conducted on ^{29}Si enriched glasses in the future.

Silicon Environment and Connectivity. Table 6 reports the Si^n distribution in the investigated glasses. In each series, Si is predominantly present as Si^4 species (>84, 78 and 73% for the PB2, MB2, and PA2 series, respectively) and Si^3 species (16, 21, and 26% for the PB2, MB2 and PA2 series, respectively), with small amounts of Si^2 species. While the Si^4 fractions extracted from the MD-generated models are roughly 3–15% higher than those deduced from NMR (Table 4), the trends are the same. With increasing x , the silicate network becomes more polymerized, reflecting the concomitant transfer of the Na^+ ions toward the anionic phosphate component. Table 6 shows that Si^4 is mainly connected to other silica tetrahedrons (1.7–1.8 for series PB2, 2.0–2.1 for series MB2, and 2.3–2.4 for series PA2) and B(IV) units (1.5–1.7 for PB2, 1.4–1.6 for MB2, and 1.2–1.5 for PA2). Si^3 units, on the other hand, have one NBO which effectively replaces one silicon neighbor in the second coordination sphere. Low amounts of B(III) species are also connected to Si^3 and Si^4 (0.3–0.7). Additionally, there are small fractions of P (up to 0.2 for glasses with larger amounts of P_2O_5) that are second neighbors to Si^4 (minimal amounts of P are

Table 6. Amounts of Si^4 , Si^3 , and Si^2 Species (in % of the Si Content) Found in the MD-Generated Glasses and Average Number of NFU Bound to Si^4 and Si^3 (± 0.1)^a

sample ID	Si^4	#B(IV)	#B(III)	#Si	#P
PB0	84.2	1.7	0.5	1.8	–
PB2-P1	86.4	1.7	0.5	1.7	0.0
PB2-P3	88.5	1.6	0.6	1.7	0.1
PB2-P5	92.3	1.5	0.7	1.7	0.2
PB3-P7	94.8	1.5	0.7	1.5	0.2
MB0	78.8	1.6	0.4	2.1	–
MB2-P1	79.6	1.5	0.4	2.1	0.1
MB2-P3	85.9	1.5	0.5	2.0	0.1
MB2-P5	89.1	1.4	0.4	2.0	0.2
PA0	73.3	1.5	0.3	2.3	–
PA2-P1	83.2	1.2	0.4	2.4	0.0
PA2-P3	80.5	1.3	0.3	2.3	0.1

sample ID	Si^2	Si^3	#B(IV)	#B(III)	#Si	#P
PB0	0.1	15.7	1.7	0.4	1.0	–
PB2-P1	0.0	13.7	1.6	0.4	1.0	0.0
PB2-P3	0.1	11.4	1.7	0.3	1.1	0.0
PB2-P5	0.0	7.7	1.5	0.4	1.1	0.0
PB3-P7	0.0	5.3	1.5	0.5	1.0	0.0
MB0	0.3	20.9	1.6	0.3	1.1	–
MB2-P1	0.3	20.1	1.6	0.2	1.2	0.0
MB2-P3	0.0	14.1	1.5	0.3	1.2	0.0
MB2-P5	0.5	10.4	1.4	0.4	1.2	0.1
PA0	1.0	25.7	1.5	0.3	1.2	–
PA2-P1	0.4	16.4	1.2	0.4	1.4	0.0
PA2-P3	0.6	18.9	1.3	0.3	1.3	0.1

^a# indicates the average number of linkages from Si^4 and Si^3 species to each NFU

observed around Si^3 units). As was also observed for B(IV) species, upon addition of P_2O_5 to the glass, the environment of Si is depleted in B(IV) and Si species and enriched in B(III) species as the B(III) units tend to link with B(IV) and Si atoms.

Phosphorus Environment: Short-Range Order. Table 7 indicates that the phosphorus speciation in the present glasses is

Table 7. Structural Speciation of Phosphorus (in % of the P Content) in the MD-Generated Glasses

sample ID	P^0 total	P^1 total	P^2 total	P^3 total	P^4 total
PB0	N/A	N/A	N/A	N/A	N/A
PB2-P1	0.0	47.5	41.5	11.0	0.1
PB2-P3	0.0	25.2	58.1	15.3	1.4
PB2-P5	0.4	20.7	60.6	17.2	1.2
PB3-P7	0.0	15.0	73.0	11.2	0.8
MB0	N/A	N/A	N/A	N/A	N/A
MB2-P1	0.0	35.4	56.7	8.0	0.0
MB2-P3	0.9	27.3	64.7	7.2	0.0
MB2-P5	0.0	19.4	68.4	11.8	0.4
PA0	N/A	N/A	N/A	N/A	N/A
PA2-P1	0.1	29.9	55.7	14.3	0.0
PA2-P3	0.9	38.4	52.6	8.3	0.0

dominated by anionic P^1 and P^2 units reflecting the well-known fact that P preferentially attracts the anionic charges in mixed network former systems. Quantitative data on this effect are shown in Figure 9. Plotted are the fractions of NBOs bound to each NFU in the three glass series studied here, not counting the uncharged formally doubly bonded NBO already present for any

t6

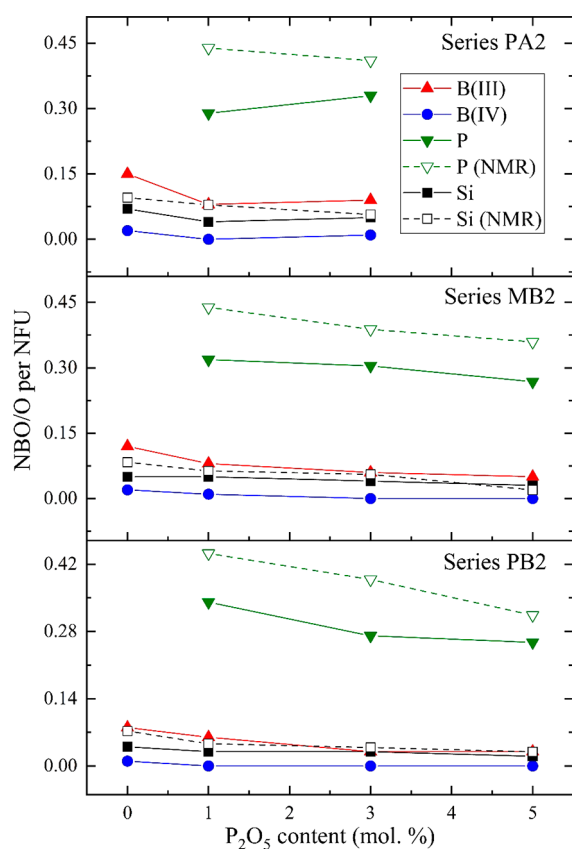


Figure 9. MD-derived average numbers of NBOs per network-forming species B(III), B(IV), Si, and P plotted as a function of x . In the case of the P and Si speciation, results from NMR are shown for comparison.

Table 8. Average Numbers of Network Former Units (B(IV), B(III), P, and Si) Connected to P¹ and P² Species in the MD-Generated Glasses^a

Sample ID	P ¹			
	#B(IV)	#B(III)	#Si	#P
PB2-P1	0.3	0.1	0.6	0.0
PB2-P3	0.3	0.1	0.6	0.0
PB2-P5	0.3	0.1	0.5	0.1
PB3-P7	0.3	0.2	0.3	0.2
MB2-P1	0.5	0.1	0.4	0.0
MB2-P3	0.2	0.2	0.6	0.0
MB2-P5	0.3	0.1	0.6	0.0
PA2-P1	0.3	0.1	0.6	0.0
PA2-P3	0.2	0.0	0.7	0.1

sample ID	P ²			
	#B(IV)	#B(III)	#Si	#P
PB2-P1	1.2	0.0	0.8	0.0
PB2-P3	1.2	0.2	0.6	0.0
PB2-P5	0.9	0.2	0.9	0.0
PB3-P7	1.0	0.2	0.7	0.1
MB2-P1	1.1	0.0	0.9	0.0
MB2-P3	1.1	0.1	0.8	0.0
MB2-P5	0.9	0.2	0.9	0.0
PA2-P1	0.9	0.2	0.9	0.0
PA2-P3	0.9	0.1	1.0	0.0

^a# indicates the average number of linkages from P¹ and P² species to each NFU

Na increases with increasing P_2O_5 content in the glass, indicating that sodium gradually shifts from its role as a charge compensator connected to boron-bonded BO species to a charge compensator of anionic nonbridging oxygen atoms attached to phosphate species. To investigate the sodium distribution around each NFU in the glass, we have plotted the T–Na (T = Si, B(III), B(IV), P) pair distribution functions in Figure S6 and compared the T–Na coordination numbers extracted from the simulations to that computed according to homogeneously distributed sodium in the glass (see Figure S7). Figure S6 indicates that the most probable Si–Na distances range between 3.3 and 3.4 Å and no particular trend is observed with P_2O_5 content apart from a slight decrease in their occurrence (evidenced by a decreased peak intensity). The B(III)–Na peak is centered at 3.0 Å and splits into two peaks (3.0 and 3.1 Å) upon P_2O_5 addition. While the B(III)–Na interaction is not traditionally expected as these units are charge-neutral, their spatial proximity can be attributed to either B²(III) units containing 1 NBO or B³(III) units linked to B(IV) units which are Na⁺ charge-compensated. The B(IV)–Na PDF peak, on the other hand, is narrower than the B(III)–Na peak and occurs at slightly shorter distances (2.9 Å), whereas the P–Na PDFs show a double peak centered at 3.1 and 3.4 Å. From the viewpoint of the Na⁺ ions, their interactions with the NFUs in the second-nearest neighbor sphere are of particular interest. For defining this sphere, a cutoff distance of 3.6 Å was found to yield stable results. Table 9 summarizes the development of the Na–NFU correlations extracted from the MD generated model. They show a clear dependence on P_2O_5 content, marked by monotonic decreases in Si, B(III), and B(IV) neighbors and increases in the number of P neighbors. Therefore, the sodium ions strongly prefer phosphate species over any other NFUs in the second coordination sphere of Na. This finding stands in

phosphate unit. The data confirm the results of a previous study of sodium calcium phospho-borosilicate glasses^{38,91} indicating that the attraction of anionic NBO decreases in the order P ≫ B(III) > Si > B(IV). The average number of bridging oxygen atoms per phosphate unit, $\langle n \rangle$ as deduced from MD is found to be somewhat higher than the corresponding experimental values determined from NMR. Nevertheless, both data sets show that $\langle n \rangle$ consistently increases with increasing x in the MB2 and PB2 glass series. In contrast, NMR and MD speciation seem to follow opposite trends in the compositionally more limited series PA2.

Phosphorus Environment: Connectivity. Table 8 summarizes the NFU connectivities of the phosphate species, indicating a dominance of Si and B(IV) units. At variance with the MAS NMR data, the MD results indicate very low levels of P–O–P linkages. One possible reason for this discrepancy can be seen in the low overall concentration of the P atoms in our glasses. As a consequence, their speciation and connectivities have little influence on the energy minimum sought in the simulation. Considering this situation, the correct prediction of the trend of $\langle n \rangle$ as a function of x and the consistent information on P–O–B linkages can already be considered a remarkable success.

Sodium Distribution. The MD simulations reveal that sodium is surrounded by an average of 6.4 and 6.5 oxygen atoms at distances near 2.40 Å in MB0 and PB0 glasses, respectively. Upon addition of P_2O_5 to each glass series, both the average Na coordination numbers and Na–O distances tend to decrease to 6.2/6.3 and 2.37 Å, respectively. The coordination numbers and distances remain almost constant at 6.2 and 2.38 Å, respectively for series PA2. Regarding the partitioning between NBO and BO in the studied glasses, the fraction of NBO around

Table 9. Contributions of P, B(III), B(IV), and Si to the Second-Nearest Neighbor Coordination of Na in the MD-Generated Glasses^a

sample ID	#P	#B(III)	#B(IV)	#Si
PB0	—	1.7	2.5	2.3
PB2-P1	0.2	1.6	2.5	2.2
PB2-P3	0.6	1.5	2.2	2.0
PB2-P5	1.0	1.4	2.0	1.7
PB3-P7	1.3	1.3	1.9	1.4
MB0	—	1.4	2.2	2.6
MB2-P1	0.2	1.3	2.2	2.6
MB2-P3	0.7	1.2	1.9	2.3
MB2-P5	1.0	1.1	1.7	2.0
PA0	—	1.0	1.9	3.0
PA2-P1	0.2	0.9	1.7	2.9
PA2-P3	0.6	0.8	1.6	2.5

^a# indicates the average number of each NFU within 3.6 Å of Na.

B³(III) species) and a considerable repolymerization of the silicate network. These changes are attributed to a significant redistribution of Na⁺ cations toward anionic phosphate NBO sites and away from silicate or borate network units. The rate of change in average P connectivity to boron ($\langle n_B(P) \rangle$) as a function of P₂O₅ content increases in the order of PA → MB → PB. The present study demonstrates that MD simulations can be used to guide and/or validate the structural interpretation of MAS NMR data. In addition, MD simulations can provide useful supplemental structural data not available from NMR studies.

6. IMPLICATIONS ON THE DESIGN OF NOVEL BOROSILICATE BIOACTIVE GLASSES

It is well-known that the short- and intermediate-range order in multicomponent glasses greatly affects the glass degradation behavior in simulated body environments. For instance, weakly bound species (i.e., Na⁺ at Si-NBO sites) are readily released from the glass in aqueous environments via ion exchange.^{93–95} Also, B(III) species (acting as Lewis acid sites) have been previously shown to react with water at quicker rates in comparison to B(IV) species.^{96–98} Furthermore, isolated orthophosphate (P⁰) units are known to be released easily from the glass and to promote biomineralization, whereas P¹_{Si} units inhibit the same bioactive processes.^{29,38,41} However, in the present phospho-borosilicate glass system, significant amounts of weakly bound isolated phosphate species (P⁰ and P¹_{1P}) in the $x = 1$ glasses are replaced by species containing P–O–B(IV) NFU linkages. The latter species, similarly as P¹_{1Si} units, are likely to improve the chemical durability of glass, thus, adversely impacting their bioactive response. Furthermore, the additional structural effects that P₂O₅ exhibits upon the NFU mixing and speciation (i.e., B(IV) and Si⁴ fractions), including its impact on the distribution and proximity of Na⁺ to specific anionic sites, can have profound effects on the ionic release characteristics and bioactivity which can benefit the conception of novel bioactive glasses for particular applications. Future studies examining *structure-degradation behavior* relationships in the present sodium phospho-borosilicate glass system can help to uncover the ideal NFU structures necessary for tuning ionic release to elicit desired biological responses when in contact with human body fluids. The described approach, which necessitates a careful compositional design, can accelerate the development of borosilicate glasses for innovative biomedical applications.

7. CONCLUSIONS

The present study combines the strengths of *state-of-the-art* experimental and computational techniques to provide a comprehensive structural understanding of the short- and intermediate-range ordering in the Na₂O–P₂O₅–B₂O₃–SiO₂ based model bioactive glass system. The impact of P₂O₅ on the structure of glasses designed in the perboric ($R < 1$), metaboric ($R = 1$), and peralkaline ($R > 1$) regions of the above-mentioned system has been investigated. While P₂O₅ > 3 mol % leads to phase separation and formation of crystalline Na₄P₂O₇ in peralkaline systems, the glass-forming ability increases with decreasing R -value. Furthermore, P₂O₅ induces repolymerization in the silicate units and a restructuring of the borate component in the glass network, which is driven by the additional demand of phosphate for charge compensation. In addition, the degree (n) of phosphate polymerization increases as a function of P₂O₅ content, as increasing amounts of B–O–P

excellent agreement with the conclusions from the ²³Na{³¹P} REDOR studies. We can put this agreement into more quantitative terms, considering that the dipolar second moments $M_{2(S-I)}$, determined experimentally by REDOR via eq 1 and listed in Table 3 follow from the internuclear distance distribution according to the van Vleck equation (eq 7),⁹²

$$M_{2(S-I)} = \frac{4}{15} \left(\frac{\mu_0}{4\pi} \right)^2 \gamma_I^2 \gamma_S^2 \hbar^2 I(I+1) \sum \frac{1}{r_{S-I}^6} \quad (7)$$

where γ_I and γ_S are the gyromagnetic ratios of the nuclear species involved, and r_{S-I} are the internuclear distances between the observed nuclei (S) and the nuclei (I) of spin quantum number I to which they are coupled, and all the other symbols have their usual meanings. As all of the constants in eq 7 are well-known, we can calculate experimental values of $\sum \frac{1}{r_{S-I}^6}$ (NMR) from the numerical second moments $M_{2(P-Na)}$ and $M_{2(Na-P)}$ listed in Table 3. This value can be compared with values of $\sum \frac{1}{r_{S-I}^6}$ extracted from the MD generated models, by extending the summation to the convergence limit, which in the present case was found to be 15 Å, and results were averaged over a total of 451 ²³Na-observe and 126 ³¹P-observe nuclei, respectively. For the glass PB3-P7, these numbers are in very good agreement: Specifically, we find $\sum \frac{1}{r_{P-Na}^6} = 3.5 \times 10^{57} \text{ m}^{-6}$ and $3.8 \times 10^{57} \text{ m}^{-6}$ from NMR and MD output, while the corresponding results for $\sum \frac{1}{r_{Na-P}^6}$ are $1.8 \times 10^{57} \text{ m}^{-6}$ and $1.1 \times 10^{57} \text{ m}^{-6}$, respectively. This preliminary result is very encouraging, showing good consistency between the MD and NMR data. Future studies will be devoted to a more systematic comparison of all the $M_{2(S-I)}$ values ($S, I = {}^{11}\text{B}, {}^{23}\text{Na}, {}^{31}\text{P}$) characterizing all the six possible pair correlations for a larger set of glasses in the Na₂O–SiO₂–B₂O₃–P₂O₅ system.

5. SUMMARY

The short- and intermediate-range structure of glasses designed in the peralkaline, metaboric, and perboric regions of the Na₂O–B₂O₃–P₂O₅–SiO₂ system has been investigated. In general, it is observed that an increase in the P₂O₅ content in the glasses produces an increase in the phosphate connectivity in the network (P²/P³ units replacing isolated P⁰/P¹ units). This is accompanied by a restructuring of the borate network (favoring

linkages are formed. The latter also serve to disperse the negative charges of the B(IV) units toward nonbridging oxygen atoms located on the phosphate species.^{87,88} The detailed analysis of ³¹P–¹¹B dipole–dipole and ³¹P–³¹P indirect spin–spin couplings on selected samples suggests a general picture of the NFU connectivity, which stands in excellent agreement with the conclusions drawn from the MD simulations and expands significantly on previous findings on bioactive P₂O₅-containing silicate and borosilicate glasses.^{30,38,91} In addition, the combined ²³Na-based double resonance experiments and the MD simulations portray a consistent and quantitative picture of the next-nearest neighbor coordination sphere of the modifier cations, featuring their preferred correlations with the phosphate component. Ultimately, the comprehensive structural details presented here will allow us to develop predictive models for dissolution kinetics and bioactivity. This will facilitate the compositional design of gene-activating borosilicate-based glasses with release kinetics that can be tailored to the specific demands of individual therapeutic applications.

■ ASSOCIATED CONTENT

■ Supporting Information

The Supporting Information is available free of charge at <https://pubs.acs.org/doi/10.1021/acs.jpcc.0c04470>.

XRD patterns of the studied glasses; supplemental single resonance MAS NMR data, PDF data for the MD-simulated glasses, Na-NFU coordination environment extracted from MD simulations, experimental parameters used for single and double resonance MAS NMR experiments, number of atoms utilized for each MD-simulated glass, interatomic potential parameters used for MD simulations, and fitting parameters and calculated fraction of each species for all ¹¹B and ³¹P MAS NMR data (PDF)

■ AUTHOR INFORMATION

Corresponding Authors

Hellmut Eckert – Institut für Physikalische Chemie, Westfälische Wilhelms-Universität Münster, D48149 Münster, Germany; São Carlos Institute of Physics, University of São Paulo, São Carlos, SP 13566-590, Brazil; orcid.org/0000-0002-6536-0117; Phone: +55-16-3373-8775; Email: eckert@ifsc.usp.br
Ashutosh Goel – Department of Materials Science and Engineering, Rutgers, The State University of New Jersey, Piscataway, New Jersey 08854, United States; orcid.org/0000-0003-0139-9503; Phone: +1-848-333-1523; Email: ag1179@soe.rutgers.edu

Authors

Nicholas Stone-Weiss – Department of Materials Science and Engineering, Rutgers, The State University of New Jersey, Piscataway, New Jersey 08854, United States; orcid.org/0000-0001-7139-1940
Henrik Bradtmüller – Institut für Physikalische Chemie, Westfälische Wilhelms-Universität Münster, D48149 Münster, Germany
Mariagrazia Fortino – Department of Chemical and Geological Sciences, University of Modena and Reggio Emilia, 41125 Modena, Italy

Marco Bertani – Department of Chemical and Geological Sciences, University of Modena and Reggio Emilia, 41125 Modena, Italy
Randall E. Youngman – Science and Technology Division, Corning Incorporated, Corning, New York 14831, United States
Alfonso Pedone – Department of Chemical and Geological Sciences, University of Modena and Reggio Emilia, 41125 Modena, Italy; orcid.org/0000-0003-3772-7222

Complete contact information is available at:
<https://pubs.acs.org/10.1021/acs.jpcc.0c04470>

Notes

The authors declare no competing financial interest.

■ ACKNOWLEDGMENTS

This material is based upon work supported by the National Science Foundation under Grant No. 1507131. The support of the Centers for Global Advancement and International Affairs (GAIA) at Rutgers University is acknowledged. H.E. and H.B. thank FAPESP for support under Grant No. 2013/07793-6. H.B. and H.E. also thank the DFG for support. The authors also thank the Characterization Sciences group at Corning Incorporated for the compositional analysis of the glasses.

■ REFERENCES

- (1) Hench, L. L.; Polak, J. M. Third-Generation Biomedical Materials. *Science* **2002**, 295 (5557), 1014–1017.
- (2) Xynos, I. D.; Hukkanen, M. V. J.; Batten, J. J.; Buttery, L. D.; Hench, L. L.; Polak, J. M. Bioglass® 45S5 Stimulates Osteoblast Turnover and Enhances Bone Formation in Vitro: Implications and Applications for Bone Tissue Engineering. *Calcif. Tissue Int.* **2000**, 67 (4), 321–329.
- (3) Xynos, I. D.; Edgar, A. J.; Buttery, L. D. K.; Hench, L. L.; Polak, J. M. Ionic Products of Bioactive Glass Dissolution Increase Proliferation of Human Osteoblasts and Induce Insulin-like Growth Factor II MRNA Expression and Protein Synthesis. *Biochem. Biophys. Res. Commun.* **2000**, 276 (2), 461–465.
- (4) Xynos, I. D.; Edgar, A. J.; Buttery, L. D. K.; Hench, L. L.; Polak, J. M. Gene-Expression Profiling of Human Osteoblasts Following Treatment with the Ionic Products of Bioglass® 45S5 Dissolution. *J. Biomed. Mater. Res.* **2001**, 55 (2), 151–157.
- (5) Clupper, D. C.; Hench, L. L. Crystallization Kinetics of Tape Cast Bioactive Glass 45S5. *J. Non-Cryst. Solids* **2003**, 318 (1–2), 43–48.
- (6) Lefebvre, L.; Chevalier, J.; Gremillard, L.; Zenati, R.; Thollet, G.; Bernache-Assolant, D.; Govin, A. Structural Transformations of Bioactive Glass 45S5 with Thermal Treatments. *Acta Mater.* **2007**, 55 (10), 3305–3313.
- (7) Boccaccini, A. R.; Chen, Q.; Lefebvre, L.; Gremillard, L.; Chevalier, J. Sintering, Crystallisation and Biodegradation Behaviour of Bioglass®-Derived Glass-Ceramics. *Faraday Discuss.* **2007**, 136, 27–44.
- (8) Bretcanu, O.; Chatzistavrou, X.; Paraskevopoulos, K.; Conradt, R.; Thompson, I.; Boccaccini, A. R. Sintering and Crystallisation of 45S5 Bioglass® Powder. *J. Eur. Ceram. Soc.* **2009**, 29 (16), 3299–3306.
- (9) Filgueiras, M. R. T.; La Torre, G.; Hench, L. L. Solution Effects on the Surface Reactions of Three Bioactive Glass Compositions. *J. Biomed. Mater. Res.* **1993**, 27 (12), 1485–1493.
- (10) Hench, L. L. The Story of Bioglass®. *J. Mater. Sci.: Mater. Med.* **2006**, 17 (11), 967–978.
- (11) Huang, W.; Day, D. E.; Kittiratanapiboon, K.; Rahaman, M. N. Kinetics and Mechanisms of the Conversion of Silicate (45S5), Borate, and Borosilicate Glasses to Hydroxyapatite in Dilute Phosphate Solutions. *J. Mater. Sci.: Mater. Med.* **2006**, 17 (7), 583–596.
- (12) Liu, X.; Rahaman, M. N.; Day, D. E. Conversion of Melt-Derived Microfibrillar Borate (13-93B3) and Silicate (45S5) Bioactive Glass in a

- 1286 Simulated Body Fluid. *J. Mater. Sci.: Mater. Med.* **2013**, 24 (3), 583–
1287 595.
- 1288 (13) Goel, A.; Rajagopal, R. R.; Ferreira, J. M. F. Influence of
1289 Strontium on Structure, Sintering and Biodegradation Behaviour of
1290 CaO-MgO-SrO-SiO₂-P₂O₅-CaF₂ Glasses. *Acta Biomater.* **2011**, 7 (11),
1291 4071–4080.
- 1292 (14) Ren, M.; Lu, X.; Deng, L.; Kuo, P. H.; Du, J. B₂O₃/SiO₂
1293 Substitution Effect on Structure and Properties of Na₂O-CaO-SrO-
1294 P₂O₅-SiO₂ Bioactive Glasses from Molecular Dynamics Simulations.
1295 *Phys. Chem. Chem. Phys.* **2018**, 20 (20), 14090–14104.
- 1296 (15) Lu, X.; Deng, L.; Kuo, P. H.; Ren, M.; Buterbaugh, I.; Du, J.
1297 Effects of Boron Oxide Substitution on the Structure and Bioactivity of
1298 SrO-Containing Bioactive Glasses. *J. Mater. Sci.* **2017**, 52 (15), 8793–
1299 8811.
- 1300 (16) Rahaman, M. N.; Day, D. E.; Sonny Bal, B.; Fu, Q.; Jung, S. B.;
1301 Bonewald, L. F.; Tomsia, A. P. Bioactive Glass in Tissue Engineering.
1302 *Acta Biomater.* **2011**, 7 (6), 2355–2373.
- 1303 (17) Balasubramanian, P.; Büttner, T.; Miguez Pacheco, V.;
1304 Boccaccini, A. R. Boron-Containing Bioactive Glasses in Bone and
1305 Soft Tissue Engineering. *J. Eur. Ceram. Soc.* **2018**, 38 (3), 855–869.
- 1306 (18) Stone-Weiss, N.; Pierce, E. M.; Youngman, R. E.; Gulbitten, O.;
1307 Smith, N. J.; Du, J.; Goel, A. Understanding the Structural Drivers
1308 Governing Glass–Water Interactions in Borosilicate Based Model
1309 Bioactive Glasses. *Acta Biomater.* **2018**, 65, 436–449.
- 1310 (19) Deshkar, A.; Ahmadzadeh, M.; Scrimshire, A.; Han, E.; Bingham,
1311 P. A.; Guillen, D.; McCloy, J.; Goel, A. Crystallization Behavior of Iron-
1312 and Boron-Containing Nepheline (Na₂O-Al₂O₃-2SiO₂) Based Model
1313 High-Level Nuclear Waste Glasses. *J. Am. Ceram. Soc.* **2019**, 102 (3),
1314 1101–1121.
- 1315 (20) Tilocca, A.; Cormack, A. N.; De Leeuw, N. H. The Structure of
1316 Bioactive Silicate Glasses: New Insight from Molecular Dynamics
1317 Simulations. *Chem. Mater.* **2007**, 19 (1), 95–103.
- 1318 (21) Tilocca, A. Structural Models of Bioactive Glasses from
1319 Molecular Dynamics Simulations. *Proc. R. Soc. London, Ser. A* **2009**,
1320 465 (2104), 1003–1027.
- 1321 (22) Elgayar, I.; Aliev, A. E.; Boccaccini, A. R.; Hill, R. G. Structural
1322 Analysis of Bioactive Glasses. *J. Non-Cryst. Solids* **2005**, 351 (2), 173–
1323 183.
- 1324 (23) Martin, R. A.; Twyman, H. L.; Rees, G. J.; Smith, J. M.; Barney, E.
1325 R.; Smith, M. E.; Hanna, J. V.; Newport, R. J. A Structural Investigation
1326 of the Alkali Metal Site Distribution within Bioactive Glass Using
1327 Neutron Diffraction and Multinuclear Solid State NMR. *Phys. Chem.*
1328 *Chem. Phys.* **2012**, 14 (35), 12105–12113.
- 1329 (24) Brauer, D. S.; Karpukhina, N.; Law, R. V.; Hill, R. G. Structure of
1330 Fluoride-Containing Bioactive Glasses. *J. Mater. Chem.* **2009**, 19 (31),
1331 5629–5636.
- 1332 (25) Lockyer, M. W. G.; Holland, D.; Dupree, R. NMR Investigation
1333 of the Structure of Some Bioactive and Related Glasses. *J. Non-Cryst.*
1334 *Solids* **1995**, 188 (3), 207–219.
- 1335 (26) Fu, Q.; Mauro, J. C.; Rahaman, M. N. Bioactive Glass
1336 Innovations Through Academia-Industry Collaboration. *Int. J. Appl.*
1337 *Glas. Sci.* **2016**, 7 (2), 139–146.
- 1338 (27) Fu, Q.; Rahaman, M. N.; Fu, H.; Liu, X. Silicate, Borosilicate, and
1339 Borate Bioactive Glass Scaffolds with Controllable Degradation Rate
1340 for Bone Tissue Engineering Applications. I. Preparation and in Vitro
1341 Degradation. *J. Biomed. Mater. Res., Part A* **2010**, 95A (1), 164–171.
- 1342 (28) Eckert, H. Structural Characterization of Bioactive Glasses by
1343 Solid State NMR. *J. Sol-Gel Sci. Technol.* **2018**, 88 (2), 263–295.
- 1344 (29) Tilocca, A.; Cormack, A. N. Structural Effects of Phosphorus
1345 Inclusion in Bioactive Silicate Glasses. *J. Phys. Chem. B* **2007**, 111 (S1),
1346 14256–14264.
- 1347 (30) Fayon, F.; Duée, C.; Poumeyrol, T.; Allix, M.; Massiot, D.
1348 Evidence of Nanometric-Sized Phosphate Clusters in Bioactive Glasses
1349 as Revealed by Solid-State ³¹P NMR. *J. Phys. Chem. C* **2013**, 117 (5),
1350 2283–2288.
- 1351 (31) Du, L.-S.; Stebbins, J. F. Site Preference and Si/B Mixing in
1352 Mixed-Alkali Borosilicate Glasses: A High-Resolution ¹¹B and ¹⁷O
1353 NMR Study. *Chem. Mater.* **2003**, 15 (20), 3913–3921.
- (32) Du, L.-S.; Stebbins, J. F. Nature of Silicon–Boron Mixing in
Sodium Borosilicate Glasses: A High-Resolution ¹¹B and ¹⁷O NMR
Study. *J. Phys. Chem. B* **2003**, 107 (37), 10063–10076.
- (33) Yun, Y. H.; Bray, P. J. Nuclear Magnetic Resonance Studies of the
Glasses in the System Na₂O-B₂O₃-SiO₂. *J. Non-Cryst. Solids* **1978**, 27,
363–380.
- (34) Dell, W. J.; Bray, P. J.; Xiao, S. Z. ¹¹B NMR Studies and Structural
Modeling of Na₂O-B₂O₃-SiO₂ Glasses of High Soda Content. *J. Non-*
Cryst. Solids **1983**, 58 (1), 1–16.
- (35) Manara, D.; Grandjean, A.; Neuville, D. R. Structure of
Borosilicate Glasses and Melts: A Revision of the Yun, Bray and Dell
Model. *J. Non-Cryst. Solids* **2009**, 355 (S0–S1), 2528–2531.
- (36) van Wüllen, L.; Müller-Warmuth, W.; Papageorgiou, D.;
Pentlinghaus, H. J. Characterization and Structural Developments of
Gel-Derived Borosilicate Glasses: A Multinuclear MAS-NMR Study. *J.*
Non-Cryst. Solids **1994**, 171 (1), 53–67.
- (37) Lee, S. K.; Musgrave, C. B.; Zhao, P.; Stebbins, J. F. Topological
Disorder and Reactivity of Borosilicate Glasses: Quantum Chemical
Calculations and ¹⁷O and ¹¹B NMR Study. *J. Phys. Chem. B* **2001**, 105
(S0), 12583–12595.
- (38) Yu, Y.; Stevensson, B.; Edén, M. Medium-Range Structural
Organization of Phosphorus-Bearing Borosilicate Glasses Revealed by
Advanced Solid-State NMR Experiments and MD Simulations:
Consequences of B/Si Substitutions. *J. Phys. Chem. B* **2017**, 121
(41), 9737–9752.
- (39) Muñoz, F.; Montagne, L.; Delevoye, L.; Durán, A.; Pascual, L.;
Cristol, S.; Paul, J. F. Phosphate Speciation in Sodium Borosilicate
Glasses Studied by Nuclear Magnetic Resonance. *J. Non-Cryst. Solids*
2006, 352 (28–29), 2958–2968.
- (40) Gan, H.; Hess, P. C.; Kirkpatrick, R. J. Phosphorus and Boron
Speciation in K₂O-B₂O₃-SiO₂-P₂O₅ Glasses. *Geochim. Cosmochim. Acta*
1994, 58 (21), 4633–4647.
- (41) Stevensson, B.; Yu, Y.; Edén, M. Structure-Composition Trends
in Multicomponent Borosilicate-Based Glasses Deduced from Molec-
ular Dynamics Simulations with Improved B-O and P-O Force Fields.
Phys. Chem. Chem. Phys. **2018**, 20 (12), 8192–8209.
- (42) Youngman, R. NMR Spectroscopy in Glass Science: A Review of
the Elements. *Materials* **2018**, 11, 476.
- (43) Gambuzzi, E.; Pedone, A.; Menziani, M. C.; Angeli, F.; Florian, P.;
Charpentier, T. Calcium Environment in Silicate and Aluminosilicate
Glasses Probed by ⁴³Ca MQMAS NMR Experiments and MD-
GIPAW Calculations. *Solid State Nucl. Magn. Reson.* **2015**, 68–69, 31–
36.
- (44) Angeli, F.; Gaillard, M.; Jollivet, P.; Charpentier, T. Contribution
of ⁴³Ca MAS NMR for Probing the Structural Configuration of Calcium
in Glass. *Chem. Phys. Lett.* **2007**, 440 (4–6), 324–328.
- (45) Christensen, R.; Byer, J.; Kaufmann, T.; Martin, S. W. Structure
– Property Relationships in the Mixed Glass Former System Na₂O–
B₂O₃–P₂O₅. *Phys. Chem. Glasses* **2009**, 50 (4), 237–242.
- (46) Hoppe, A.; Güldal, N. S.; Boccaccini, A. R. A Review of the
Biological Response to Ionic Dissolution Products from Bioactive
Glasses and Glass-Ceramics. *Biomaterials* **2011**, 32 (11), 2757–2774.
- (47) Jeznach, O.; Gajc, M.; Korzeb, K.; Kłos, A.; Orliński, K.; Stępień,
R.; Krok-Borkowicz, M.; Rumian, Ł.; Pietryga, K.; Reczyńska, K.;
Pamula, E.; Pawlak, D. A. New Calcium-Free Na₂O–Al₂O₃–P₂O₅
Bioactive Glasses with Potential Applications in Bone Tissue
Engineering. *J. Am. Ceram. Soc.* **2018**, 101 (2), 602–611.
- (48) Sriranganathan, D.; Kanwal, N.; Hing, K. A.; Hill, R. G.
Strontium Substituted Bioactive Glasses for Tissue Engineered
Scaffolds: The Importance of Octacalcium Phosphate. *J. Mater. Sci.: Mater. Med.* **2016**, 27 (2), 1–10.
- (49) Wu, C.; Fan, W.; Gelinsky, M.; Xiao, Y.; Simon, P.; Schulze, R.;
Doert, T.; Luo, Y.; Cuniberti, G. Bioactive SrO-SiO₂ Glass with Well-
Ordered Mesopores: Characterization, Physicochemistry and Biological
Properties. *Acta Biomater.* **2011**, 7 (4), 1797–1806.
- (50) Weitzmann, M. N.; Ha, S. W.; Vikulina, T.; Roser-Page, S.; Lee, J.
K.; Beck, G. R. Bioactive Silica Nanoparticles Reverse Age-Associated
Bone Loss in Mice. *Nanomedicine* **2015**, 11 (4), 959–967.

- (51) Ha, S. W.; Weitzmann, M. N.; Beck, G. R. Bioactive Silica Nanoparticles Promote Osteoblast Differentiation through Stimulation of Autophagy and Direct Association with LC3 and P62. *ACS Nano* **2014**, *8* (6), 5898–5910.
- (52) Hidi, I. J.; Melinte, G.; Stefan, R.; Bindea, M.; Baia, L. The Study of the Structure and Bioactivity of the $B_2O_3 \bullet Na_2O \bullet P_2O_5$ System. *J. Raman Spectrosc.* **2013**, *44* (8), 1187–1194.
- (53) Magyari, K.; Stefan, R.; Vodnar, D. C.; Vulpoi, A.; Baia, L. The Silver Influence on the Structure and Antibacterial Properties of the Bioactive $10B_2O_3 \cdot 30Na_2O \cdot 60P_2O_5$ Glass. *J. Non-Cryst. Solids* **2014**, *402*, 182–186.
- (54) Magyari, K.; Stefan, R.; Vulpoi, A.; Baia, L. Bioactivity Evolution of Calcium-Free Borophosphate Glass with Addition of Titanium Dioxide. *J. Non-Cryst. Solids* **2015**, *410*, 112–117.
- (55) Martens, R.; Müller-Warmuth, W. Structural Groups and Their Mixing in Borosilicate Glasses of Various Compositions - an NMR Study. *J. Non-Cryst. Solids* **2000**, *265* (1), 167–175.
- (56) Mazurin, O.; Streltsina, M. V.; Shvaiko-Shvaikovskaya, T. P. *Sci. Glass-6.5 (Glass Property Information System)*; Institute of Theoretical Chemistry, Shrewsbury, MA, 2005.
- (57) Lesage, A.; Bardet, M.; Emsley, L. Through-Bond Carbon-Carbon Connectivities in Disordered Solids by NMR. *J. Am. Chem. Soc.* **1999**, *121* (47), 10987–10993.
- (58) Ren, J.; Eckert, H. Quantification of Short and Medium Range Order in Mixed Network Former Glasses of the System GeO_2 - $NaPO_3$: A Combined NMR and X-ray Photoelectron Spectroscopy Study. *J. Phys. Chem. C* **2012**, *116* (23), 12747–12763.
- (59) Massiot, D.; Fayon, F.; Capron, M.; King, L.; Le Calvé, S.; Alonso, B.; Durand, J. O.; Bujoli, B.; Gan, Z.; Hoatson, G. Modelling One- and Two-Dimensional Solid-State NMR Spectra. *Magn. Reson. Chem.* **2002**, *40* (1), 70–76.
- (60) Massiot, D.; Bessada, C.; Coutures, J. P.; Taulelle, F. A Quantitative Study of ^{27}Al MAS NMR in Crystalline YAG. *J. Magn. Reson.* **1990**, *90* (2), 231–242.
- (61) Chan, J. C. C.; Eckert, H. Dipolar Coupling Information in Multispin Systems: Application of a Compensated REDOR NMR Approach to Inorganic Phosphates. *J. Magn. Reson.* **2000**, *147* (2), 170–178.
- (62) Gullion, T. Measurement of Heteronuclear Dipolar Interactions by Rotational-Echo, Double-Resonance Nuclear Magnetic Resonance. **1998**.
- (63) Bertmer, M.; Eckert, H. Dephasing of Spin Echoes by Multiple Heteronuclear Dipolar Interactions in Rotational Echo Double Resonance NMR Experiments. *Solid State Nucl. Magn. Reson.* **1999**, *15*, 139–152.
- (64) Schulze, G. E. R. Die Kristallstruktur von BPO_4 Und $BAsO_4$. *Naturwissenschaften* **1933**, *21* (30), 562.
- (65) Ondik, H. M. The Structure of Anhydrous Sodium Trimetaphosphate $Na_3P_3O_9$, and the Monohydrate, $Na_3P_3O_9 \cdot H_2O$. *Acta Crystallogr.* **1965**, *18* (2), 226–232.
- (66) Ba, Y.; Kao, H. M.; Grey, C. P.; Chopin, L.; Gullion, T. Optimizing the ^{13}C - ^{14}N REAPDOR NMR Experiment: A Theoretical and Experimental Study. *J. Magn. Reson.* **1998**, *133* (1), 104–114.
- (67) Bak, M.; Rasmussen, J. T.; Nielsen, N. C. SIMPSON: A General Simulation Program for Solid-State NMR Spectroscopy. *J. Magn. Reson.* **2011**, *213* (2), 366–400.
- (68) Pedone, A. Properties Calculations of Silica-Based Glasses by Atomistic Simulations Techniques: A Review. *J. Phys. Chem. C* **2009**, *113* (49), 20773–20784.
- (69) Tilocca, A.; De Leeuw, N. H.; Cormack, A. N. Shell-Model Molecular Dynamics Calculations of Modified Silicate Glasses. *Phys. Rev. B: Condens. Matter Mater. Phys.* **2006**, *73* (10), 104209.
- (70) Tilocca, A. Short- and Medium-Range Structure of Multi-component Bioactive Glasses and Melts: An Assessment of the Performances of Shell-Model and Rigid-Ion Potentials. *J. Chem. Phys.* **2008**, *129* (8), 084504.
- (71) Fortino, M.; Berselli, A.; Stone-Weiss, N.; Deng, L.; Goel, A.; Du, J.; Pedone, A. Assessment of Interatomic Parameters for the Reproduction of Borosilicate Glass Structures via DFT-GIPAW Calculations. *J. Am. Ceram. Soc.* **2019**, *102* (12), 7225–7243.
- (72) Pedone, A.; Malavasi, G.; Menziani, M. C. Computational Insight into the Effect of CaO/MgO Substitution on the Structural Properties of Phospho-Silicate Bioactive Glasses. *J. Phys. Chem. C* **2009**, *113* (35), 15723–15730.
- (73) Sanders, M. J.; Leslie, M.; Catlow, C. R. A. Interatomic Potentials for SiO_2 . *J. Chem. Soc., Chem. Commun.* **1984**, No. 19, 1271–1273.
- (74) Smith, W.; Forester, T. R. DL-POLY-2.0: A General-Purpose Parallel Molecular Dynamics Simulation Package. *J. Mol. Graphics* **1996**, *14* (3), 136–141.
- (75) Segall, M. D.; Lindan, P. J. D.; Probert, M. J.; Pickard, C. J.; Hasnip, P. J.; Clark, S. J.; Payne, M. C. First-Principles Simulation: Ideas, Illustrations and the CASTEP Code. *J. Phys.: Condens. Matter* **2002**, *14* (11), 2717–2744.
- (76) Pickard, C. J.; Mauri, F. All-Electron Magnetic Response with Pseudopotentials: NMR Chemical Shifts. *Phys. Rev. B: Condens. Matter Mater. Phys.* **2001**, *63* (24), 245101.
- (77) Han, F. Projector-Augmented Plane-Wave Method. *Probl. Solid State Phys. with Solut.* **2011**, *50* (24), 391–396.
- (78) Tasker, P. W. The Stability of Ionic Crystal Surfaces. *J. Phys. C: Solid State Phys.* **1979**, *12* (22), 4977.
- (79) Pedone, A.; Charpentier, T.; Malavasi, G.; Menziani, M. C. New Insights into the Atomic Structure of 45SS Bioglass by Means of Solid-State NMR Spectroscopy and Accurate First-Principles Simulations. *Chem. Mater.* **2010**, *22* (19), S644–S652.
- (80) Alderman, O. L. G.; Iuga, D.; Howes, A. P.; Pike, K. J.; Holland, D.; Dupree, R. Spectral Assignments and NMR Parameter-Structure Relationships in Borates Using High-Resolution ^{11}B NMR and Density Functional Theory. *Phys. Chem. Chem. Phys.* **2013**, *15* (21), 8208–8221.
- (81) Gambuzzi, E.; Charpentier, T.; Menziani, M. C.; Pedone, A. Computational Interpretation of ^{23}Na MQMAS NMR Spectra: A Comprehensive Investigation of the Na Environment in Silicate Glasses. *Chem. Phys. Lett.* **2014**, *612*, 56–61.
- (82) Pyykko, P. Year-2008 Nuclear Quadrupole Moments. *Mol. Phys.* **2008**, *106* (16–18), 1965–1974.
- (83) Presti, D.; Pedone, A.; Licari, D.; Barone, V. A Modular Implementation for the Simulation of 1D and 2D Solid-State NMR Spectra of Quadrupolar Nuclei in the Virtual Multifrequency Spectrometer-Draw Graphical Interface. *J. Chem. Theory Comput.* **2017**, *13* (5), 2215–2229.
- (84) Feller, S. A.; Kottke, J.; Welter, J.; Nijhawan, S.; Boekenhauer, R.; Zhang, H.; Feil, D.; Parameswar, C.; Budhwani, K.; Affatigato, M. Physical Properties of Alkali Borosilicate Glasses. *Proceedings of the Second International Conference on Borate Glasses, Crystals, and Melts, Abingdon, United Kingdom; Sheffield (United Kingdom): The Society of Glass Technology* **1997**, 246–253.
- (85) Du, L. S.; Stebbins, J. F. Solid-State NMR Study of Metastable Immiscibility in Alkali Borosilicate Glasses. *J. Non-Cryst. Solids* **2003**, *315* (3), 239–255.
- (86) Bertmer, M.; Züchner, L.; Chan, J. C. C.; Eckert, H. Short and Medium Range Order in Sodium Aluminoborate Glasses. 2. Site Connectivities and Cation Distributions Studied by Rotational Echo Double Resonance NMR Spectroscopy. *J. Phys. Chem. B* **2000**, *104* (28), 6541–6553.
- (87) Funke, L. M.; Eckert, H. Charge Compensation in Sodium Borophosphate Glasses Studied by $^{11}B\{^{23}Na\}$ and $^{31}P\{^{23}Na\}$ Rotational Echo Double Resonance Spectroscopy. *J. Phys. Chem. C* **2016**, *120* (6), 3196–3205.
- (88) Larink, D.; Eckert, H.; Reichert, M.; Martin, S. W. Mixed Network Former Effect in Ion-Conducting Alkali Borophosphate Glasses: Structure/Property Correlations in the System $[M_2O]_{1/3}[(B_2O_3)_x(P_2O_5)_{1-x}]_{2/3}$ ($M = Li, K, Cs$). *J. Phys. Chem. C* **2012**, *116* (50), 26162–26176.
- (89) El-Damrawi, G.; Müller-Warmuth, W.; Doweidar, H.; Gohar, I. A. Structure and Heat Treatment Effects of Sodium Borosilicate Glasses as Studied by ^{29}Si and ^{11}B NMR. *J. Non-Cryst. Solids* **1992**, *146*, 137–144.

- (90) Martin, S. W.; Bhatnagar, A.; Parameswar, C.; Feller, S.; MacKenzie, J. ^{29}Si MAS-NMR Study of the Short-Range Order in Potassium Borosilicate Glasses. *J. Am. Ceram. Soc.* **1995**, *78* (4), 952–960.
- (91) Yu, Y.; Edén, M. Structure-Composition Relationships of Bioactive Borophosphosilicate Glasses Probed by Multinuclear ^{11}B , ^{29}Si , and ^{31}P Solid State NMR. *RSC Adv.* **2016**, *6* (103), 101288–101303.
- (92) Van Vleck, J. H. Dipolar Broadening of Magnetic Resonance Lines in Crystals. *Phys. Rev.* **1948**, *74* (9), 1168.
- (93) Perera, G.; Doremus, R. H. Dissolution Rates of Commercial Soda-Lime and Pyrex Borosilicate Glasses: Influence of Solution pH. *J. Am. Ceram. Soc.* **1991**, *74* (7), 1554–1558.
- (94) Bunker, B. C. Molecular Mechanisms for Corrosion of Silica and Silicate Glasses. *J. Non-Cryst. Solids* **1994**, *179*, 300–308.
- (95) Hamilton, J. P.; Pantano, C. G. Effects of Glass Structure on the Corrosion Behavior of Sodium-Aluminosilicate Glasses. *J. Non-Cryst. Solids* **1997**, *222*, 167–174.
- (96) Kapoor, S.; Youngman, R. E.; Zakharchuk, K.; Yaremchenko, A.; Smith, N. J.; Goel, A. Structural and Chemical Approach toward Understanding the Aqueous Corrosion of Sodium Aluminoborate Glasses. *J. Phys. Chem. B* **2018**, *122* (48), 10913–10927.
- (97) Brauer, D. S.; Möncke, D. Introduction to the Structure of Silicate, Phosphate and Borate Glasses. *Bioactive Glasses* **2016**, 61–88.
- (98) Abdelghany, A. M. Novel Method for Early Investigation of Bioactivity in Different Borate Bio-Glasses. *Spectrochim. Acta, Part A* **2013**, *100*, 120–126.